Modeling firn densification through viscosity and microstructures

Brita Ilyse Horlings

A thesis

submitted in partial fulfillment of the

requirements for the degree of

Master of Science

University of Washington

2019

Committee:

Ed Waddington, Chair

T.J. Fudge

Program Authorized to Offer Degree:

Earth and Space Sciences

University of Washington

Abstract

Modeling firn densification through viscosity and microstructures

Brita I. Horlings

Chair of Supervisory Committee:
Edwin D. Waddington
Earth and Space Sciences

Knowledge of firn densification is important for several applications, such as for ice-sheet surface elevation changes from repeat satellite altimetry methods used to estimate ice-sheet contribution to sea-level rise. Uncertainties in firn-densification rates are among the largest uncertainties for this method mainly because most commonly-used firn-densification models are empirically constructed for estimating the macroscopic behavior of the firn. Currently, no model that is either fully physically-based or is applicable to the entire firn column exists.

First, we examine the implicit effective viscosity for models within the Community Firn Model (CFM) under a range of climatic conditions, and find that there exist physically unrealistic discontinuities in viscosity at the transitional density of 550 kg m^{-3}. To generate a continuous viscosity curve, we develop a transition model that gradually transitions processes in zone 1 to those in zone 2 of the firn layer. We use the transition model for estimating depth-density for a range of climates, and we generally see that the transition model shows lower RMSE values compared to the Herron and Langway (1980) model for climatic sites that do not have a regular Clausius-Clapeyron pairing of temperature and accumulation rate, or sites that are influenced by other factors (e.g., horizontal strain, wind). However, the results highlight the limitations of constructing a model empirically.

Next, we develop a model that modifies a relationship from previous work to estimate the densification rate through viscosity and the evolution of microstructures. We define microstructural evolution by using micro-CT data from USP50 near South Pole, and run our model for USP50 as well as several other sites. Our results show good agreement; however, more work is necessary to further develop this model, including the collection of more microstructure data. Nevertheless, our research provides a key step towards producing a firn-densification model that estimates firn properties on the microscale and that can potentially be used in a range of climatic conditions and during climate transients.

TABLE OF CONTENTS

LIST OF FIGURES

LIST OF TABLES

Chapter 1. INTRODUCTION

Ice loss from the polar ice sheets has significantly increased the rate of sea-level rise since the 1990s and is threatening many coastal communities (IPCC, 2013). Estimation of the ice-sheet contribution to sea-level rise based on measurements of ice-sheet surface elevation changes through repeat satellite altimetry requires corrections for firn densification (changing air content), bed elevation changes, ice dynamics, and melting and accumulation. Currently, uncertainties in firn-densification rates derived from models are among the largest uncertainties for this method (Shepherd et al., 2012).

Accurately modeling firn densification requires assumptions of the feedbacks that govern compaction, and the knowledge of spatial and temporal conditions across Antarctica and Greenland. The climate (e.g., temperature, accumulation rate, and wind) of a site drive the grain-scale processes that govern firn densification in the firn layer. The densification process is typically divided into three zones based on the dominant mechanism in each zone (Herron and Langway, 1980). Grain settling and grain growth are assumed to dominate up to 550 kg m^{-3} (zone 1); sintering and grain deformation until 830 kg m^{-3} (zone 2); and bubble compression at densities greater than 830 kg m^{-3} (zone 3) (Herron and Langway, 1980).

We have a poor understanding of how the current generation of firn-densification models performs when they are used in a transient climate or outside the range in which they were calibrated (Lundin et al., 2017). The models are primarily empirical and aim to capture the macroscale behavior of the firn column; most do not incorporate physics that describe microscale evolution. Thus, one challenge in the firn research community is developing a microphysically-based model that can simulate densification over a range of climate conditions and during a changing climate. However, this requires extensive knowledge of how microscale evolution is

connected to macroscale behavior, on which many studies have focused (e.g., Alley, 1987; Wilkinson and Ashby, 1975) but have failed to produce a commonly-used, accurate firn-densification model applicable to the entire firn column and through changing conditions.

In Chapter 2, we explore the framework and inherent assumptions of a few commonly-used firn-densification models by analyzing implicitly-defined effective viscosity and an unrealistic viscosity discontinuity that exists at the zone 1 – zone 2 transition (550 kg m^{-3}). To maintain a continuous viscosity curve, we construct a model that gradually transitions zone 1 processes to zone 2 processes in the transition region around 550 kg m^{-3}. Finally, in Chapter 3, we derive a model based on microstructural evolution using micro-CT data from USP50, a site near South Pole.

Chapter 2. EFFECTIVE VISCOSITY IN FIRN-DENSIFICATION MODELS

This chapter is intended for submission to Journal of Glaciology. Author list is Brita I., Horlings[1], Edwin D. Waddington[1], T.J. Fudge[1], and C. Max Stevens[1], [1]Department of Earth and Spaces Sciences, University of Washington, WA, USA.

2.1 ABSTRACT

Uncertainties in firn-densification rates derived from models are among the largest uncertainties in ice-sheet mass loss estimates from repeat satellite altimetry. Most existing firn-densification models are empirical, and tend to perform poorly when applied outside their climate calibration range and during changes in climatic conditions. We use the Community Firn Model (CFM) to find the implicit effective viscosity from several commonly-used firn-densification models under a range of climate conditions. The principal findings are: 1) discontinuities in viscosity exist at the transitional density between zone 1 to zone 2 (550 kg m^{-3}) in the firn layer; 2) the largest fractional viscosity discontinuities are at warm sites; and 3) some low-accumulation sites show a decrease in viscosity from zone 1 to zone 2. We develop a method for ensuring continuous viscosity by applying a linear transition formulated from the densification relations defined by the Herron and Langway (1980) model. When the range and center of the transition zone are tuned accordingly, we can match depth-density profiles more closely than the Herron and Langway (1980) model, suggesting that densification mechanisms may gradually decrease or increase in dominance through the transition zone. Our work also highlights the limitations of empirical approaches to firn densification and motivates continued work on more physically-based firn-densification models.

2.2 INTRODUCTION

2.2.1 IMPORTANCE

Ice loss from the polar ice sheets has significantly increased the rate of sea-level rise since the 1990s and is threatening many coastal communities (IPCC, 2013). Estimation of ice-sheet contribution to sea-level rise by repeat satellite altimetry requires corrections to ice-sheet elevation changes from processes such as firn densification, bed elevation changes, ice dynamics, melt, and accumulation. Currently, uncertainties in firn-densification rates are among the largest uncertainties in ice-sheet mass loss estimates from repeat-satellite altimetry (Shepherd et al., 2012). Most firn-densification models were empirically constructed and aim at capturing the macroscale behavior of the firn column; they do not incorporate physics that describe processes at the microscale. Further, models are often tuned to a limited range of climates even if they are not regionally limited. Many models assume steady state by tuning compaction rates to modern depth-density profiles, which are considered to be in steady-state (e.g., Herron and Langway, 1980). We have a poor understanding of how these models perform 1) outside their climate calibration range and 2) during changes in climatic conditions (Lundin et al., 2017).

2.2.2 CURRENT MODEL FRAMEWORK

The current generation of firn-densification models simulate the evolution of firn density in one dimension using a climate forcing (typically surface temperature, accumulation rate, and surface density) and varying complexities of physics that define the rate at which the firn densifies. The densification rate $D\rho/Dt$ is derived from the volumetric strain rate $\dot{\varepsilon}$ by using the material-following definition of strain rate in Equation (1), i.e.,

$$\dot{\varepsilon} = -\frac{1}{\rho}\frac{D\rho}{Dt} < 0 \quad (1)$$

Many firn-densification relations are based on Robin's (1958) suggestion that the fractional change in porosity is proportional to the increase in overburden load. This is a steady-state assumption because it assumes that the compaction rate depends on the incremental overburden load; however, in a transient firn column, the fractional change in porosity likely depends on the total overburden load rather than on each incremental increase. Robin's (1958) suggestion is incorporated in the most-commonly used version of the equation (Equation (2)), where ρ_0 represents the smoothed density of the depth-density profile (Morris et al., 2017).

$$\dot{\varepsilon} = c\left(\frac{\rho_i - \rho_0}{\rho_0}\right) \tag{2}$$

Combining Equations (1) and (2), we get Equation (3).

$$\frac{D\rho}{Dt} = c\,(\rho_i - \rho) \tag{3}$$

Equation (3) is the foundational equation that most widely-used firn-densification relations use. The model-specific constant *c* is commonly divided into an accumulation rate-dependent term and a temperature-dependent term that are tuned using firn data from one or a number of sites (e.g., Herron and Langway, 1980; Arthern et al., 2010; Ligtenberg et al., 2011). These terms are, for example, defined through Arrhenius relationships and various physics that attempt to describe one or more physical processes. The resulting *c* is commonly adjusted according to firn density ranges, where two different zones of the firn layer are generally defined: zone 1, where grain settling and grain growth are thought to dominate ($\rho_{surface} < \rho \leq$ 550 kg m^{-3}), and zone 2, where sintering is thought to dominate (550 kg m^{-3} $< \rho \leq$ 830 kg m^{-3}).

Most firn-densification relations also use Sorge's Law, which assumes the depth-density profile is in a steady state (Arthern et al., 2010). Thus, if vertical velocity $v(z)$ is written as $v(z) = A/\rho(z)$, where *A* is the accumulation rate, then the strain rate $\dot{\varepsilon}$ can be approximated by (e.g., Bader, 1960; Herron and Langway, 1980; Arthern et al., 2010):

$$\dot{\varepsilon} \approx -\left(\frac{D\rho}{Dt}\right)\frac{A}{\rho^2} \tag{4}$$

Most firn-densification models (e.g., Herron and Langway (1980); Arthern et al., 2010; Li and Zwally, 2011; Ligtenberg, 2011) derive unique relations for zone 1 and zone 2. Such models assume that the transition occurs at the "critical density" of 550 kg m^{-3}. This boundary corresponds to the random-closest-packing density of isometric spheres where grain settling is assumed to no longer be the main contributor to densification (Alley, 1987; Anderson and Benson, 1963). However, in reality, firn grains are far from spherical or isometric, as seen, for example, from photographs or firn micro-CT data (e.g., Anderson and Benson, 1963; Gregory et al., 2014). For example, Benson's (1962) measurements show that the critical density ranges from relative densities of 0.62 to 0.56 for temperatures from 257.15 K to 243.15 K. In addition, more recent research has established that the transition from zone 1 to zone 2 may be gradual rather than abrupt (e.g., Hörhold et al., 2011; Morris, 2018).

The common firn-densification model framework fails to incorporate descriptions of relevant physical processes that change firn viscosity (e.g., the evolution of microstructural properties). In the macroscale framework, instead of being explicitly incorporated, those processes are being 'mapped' onto other parameters in the firn-densification equation. This tuning may estimate the densification rate (and effective viscosity) adequately in climates in which the model was tuned, but may not predict densification in other climate regimes where the relative importance of physical processes may differ. In this chapter, we reformulate several firn-densification models in terms of strain rate, stress, and effective viscosity. We show that when a modeling framework defines zone 1 and zone 2 with distinct equations, unrealistic discontinuities exist at that boundary. Viscosity should be a continuous function of density when modeled macroscopically even though, on a microscale, small variations in microstructure

should produce variations and discontinuities in viscosity. Our results suggest that commonly-used firn-densification models do not always incorporate important processes in the firn layer near 550 kg m^{-3}, which is a result of those models' macroscopic focuses. We create a simple transition model to produce a continuous effective viscosity within the Herron and Langway (1980) model.

2.3 METHODS

2.3.1 DERIVING EFFECTIVE VISCOSITY FROM FIRN-DENSIFICATION MODELS

We approach the problem using a continuum-mechanics framework. In this framework, firn has an effective viscosity η that relates the overburden stress σ to the strain rate $\dot{\varepsilon}$:

$$\dot{\varepsilon} = \frac{1}{2\eta}\sigma \tag{5}$$

We refer to effective viscosity simply as viscosity for the rest of the paper. By substituting Equation (1) into Equation (5) and rearranging, we obtain a relationship between a firn layer's densification rate and its viscosity:

$$\eta = -\frac{\rho\sigma}{2}\left(\frac{D\rho}{Dt}\right)^{-1} \tag{6}$$

We employ Equation (6) and the densification rate unique to each firn-densification model (Equation (3)) to extract the firn viscosity implied by each model, which we refer to as implicit viscosity. We then compare these implicit viscosities from different models and across climate conditions.

As an example, the Lagrangian densification rate in zone 1 given by the Herron and Langway (1980) model is

$$\frac{D\rho}{Dt} = k_1 \exp\left(\frac{-E_1}{RT}\right) A(\rho_i - \rho) \tag{7}$$

where k_1 is a coefficient, R is the gas constant, T is temperature, and A is the accumulation rate. The overburden stress is often written in terms of accumulation rate A since each firn parcel was deposited and parameterized as accumulation in a steady state climate

$$\sigma(t,\tau) = -g\int_{t-\tau}^{t} A(t')dt' = -g\bar{A}(t,\tau)\tau \tag{8}$$

where τ is the age of the a firn parcel and g is gravity. Combining Equations (1), (5), and (7), we get:

$$\frac{1}{\rho}\frac{D\rho}{Dt} = \frac{k_1}{g\tau}\exp\left(\frac{-E_1}{RT}\right)\frac{(\rho_i-\rho)}{\rho}\sigma(t,\tau) \tag{9}$$

Rearranging Equation (9), the viscosity that is implied by the densification rate relation of Herron and Langway (1980) is $\eta_1(t,\tau)$.

$$\eta_1(t,\tau) = \frac{g}{2k_1}\exp\left(\frac{E_1}{RT}\right)\frac{\rho}{(\rho_i-\rho)}\tau \tag{10}$$

The implicit viscosity relation for zone 2 from Herron and Langway (1980) can be similarly formulated as

$$\eta_2(t,\tau) = \frac{\sqrt{g}}{2k_2}\exp\left(\frac{E_2}{RT}\right)\frac{\rho}{(\rho_i-\rho)}\sqrt{\tau}\sqrt{\sigma}\,. \tag{11}$$

2.3.2 DISCONTINUITY AT THE ZONE 1 – ZONE 2 TRANSITION

The viscosities implicit in numerous previously published models will have the general form of Equation (6), but will differ slightly due to differences in how each model describes $\frac{D\rho}{Dt}$. Models with densification rates defined separately in zone 1 and 2 will produce an η_1 and η_2 with different functional forms. Equations (10) and (11) from the Herron and Langway (1980) model and the corresponding viscosity equations for other models show that the effective viscosity depends on such physical controls (e.g., temperature, stress, density) and proxies for controls (e.g., gravity, firn age) onto which the effect of processes on densification are being

mapped. Because of the different functional forms used in zone 1 versus zone 2, η_1 and η_2 are not necessarily equal at the 550 kg m^{-3} boundary. We assess the magnitude of this discontinuity between models and across climates.

2.4 RESULTS

2.4.1 COMPARATIVE DISCONTINUITIES ACROSS MODELS AND CLIMATES

The viscosity versus density profiles predicted by the CFM firn-densification models using a forcing of South Pole (T = 224 K, A = 6.37 cm water a^{-1}) climatic conditions is shown in Figure 2.1. The viscosity approaches infinity at a density of 917 kg m^{-3} because Equation (6) requires the densification rates to be greater than zero. Although all models show generally increasing viscosity for increasing density, the values and slopes of the curves differs. For all models that define densification separately in zone 1 and zone 2, there is a discontinuity in the viscosity at the boundary between these zones at 550 kg m^{-3}; the largest discontinuity in this case is $1.1 \cdot 10^{15}$ Pa·s (Figure 2.1).

Figure 2.2a shows viscosity profiles from the Herron and Langway (1980) model for six sites with climatic conditions described in Table 1. The magnitude of the viscosity discontinuity varies depending on the climate conditions. In general, the larger discontinuities occur for lower temperature/lower accumulation sites while smaller discontinuities occur for lower temperature/higher accumulation sites. However, this relationship excludes sites such as Taylor Mouth, where the accumulation rate is much less than expected for the temperature and does not follow the Clausius-Clapeyron relationship. At Taylor Mouth, the modeled viscosity decreases by $-1.1 \cdot 10^{14}$ Pa s from zone 1 to zone 2 despite an increase in density. This decrease across the boundary becomes larger as the accumulation received at a site gets lower, as seen from the 20 N

curve in Figure 2.2b. Other sites that do not follow the Clausius-Clapeyron curve show negative or larger positive discontinuities compared to those associated sites that do. For example, Station 524 is a relatively high-accumulation but low-temperature site, and, from Figure 2.2c, the viscosity discontinuity for Station 524 has a value of $4.3 \cdot 10^{14}$ Pa·s. Compared to those for Mile 60 and Mile 927, which both experience higher temperature, the discontinuity at Station 524 is larger.

Table 1. The climate regime (temperature T, ice-equivalent accumulation rate $\bar{b}$) for sites in Antarctica and Greenland (Spencer et al., 2001; Morse et al., 1999).

Site	T(K)	A(cm a^{-1})
Camp Century	249	36.7
Byrd	245	15.6
Mizuho G6	236	10
Mile 927	249	17.1
Mile 60	244	17.4
Taylor Dome	~233	
10 S	233.6	27
20 S	231.8	7.9
20 C	232.1	6.7
TM	236.7	2.3
20 N	234.1	1.3
Station 524	229	17.1
South Pole	224	6.37
Dome C	219.5	3.4
Vostok	216	2.2

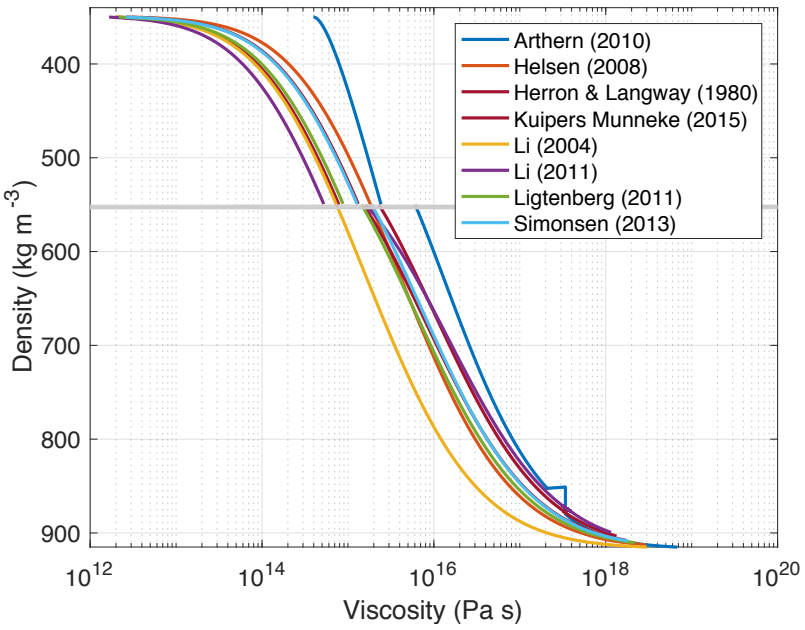

Figure 2.1. Viscosity-density curves from models of the CFM forced with temperature (224 K) and accumulation rate (6.37 cm a^{-1}) near South Pole.

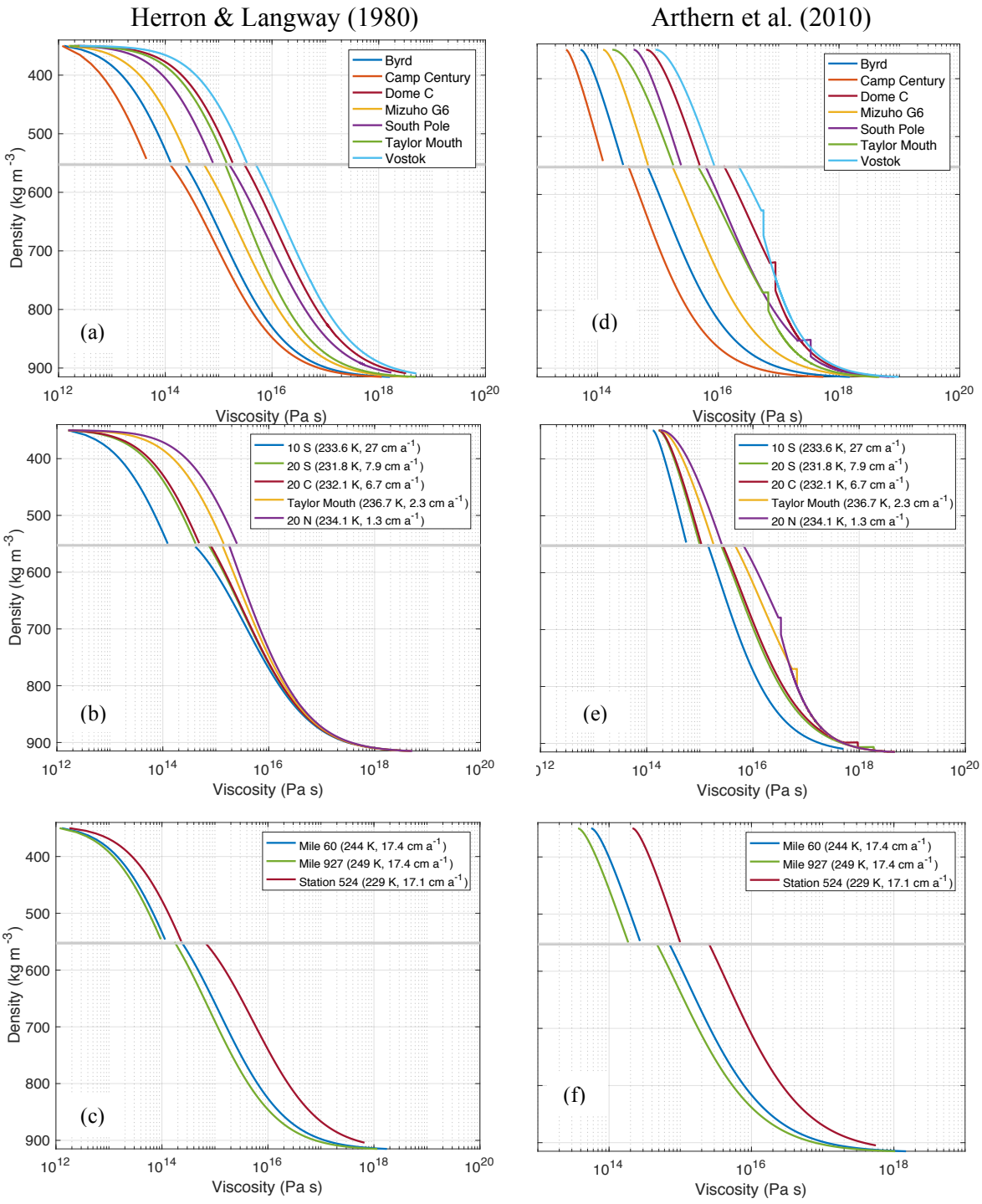

Figure 2.2. The viscosity predicted by the Herron and Langway (1980) model. (a) Sites with a range of climatic conditions around Antarctica and Greenland; (b) sites with a range of accumulation rate and very similar temperature, and (c) sites with a range of temperature but similar accumulation rate; the viscosity predicted by the Arthern et al. (2010) model (d) for sites with a range of climatic conditions around Antarctica and Greenland; (e) sites with a range of accumulation rate and very similar temperature, and (f) varying temperature but similar accumulation rate.

2.4.2 NONDIMENSIONAL VISCOSITY DISCONTINUITY

The models predict that the magnitude of the viscosity discontinuity is larger at lower-temperature, lower-accumulation sites than at higher-temperature, high-accumulation sites; however, the viscosity is also larger at these sites. Although strain rate is important, fractional differences in strain rate along a depth profile are of paramount importance. Treating firn as a viscous material, it is easy to see from a viscous constitutive relation that at constant stress σ_0, fractional differences in strain rate are directly related to fractional differences in viscosity, i.e.

$$2\,\eta_0\dot{\varepsilon}_0\left(1+{\Delta\eta}/{\eta_0}\right)\left(1+{\Delta\dot{\varepsilon}}/{\dot{\varepsilon}_0}\right)=\ \sigma_0 \tag{12}$$

After dividing through by σ_0,

$$\left(1+{\Delta\eta}/{\eta_0}\right)\left(1+{\Delta\dot{\varepsilon}}/{\dot{\varepsilon}_0}\right)=1 \tag{13}$$

Expanding the product and neglecting second-order terms,

$${\Delta\eta}/{\eta_0}+{\Delta\dot{\varepsilon}}/{\dot{\varepsilon}_0}=0 \tag{14}$$

The implicit firn viscosity also varies widely due to climatic conditions (e.g., firn is more viscous in cold climates), so we will also consider the nondimensional or fractional mismatch, which we define by scaling the viscosity difference by the zone 2 viscosity at the transition.

$$R_\eta=\frac{(\eta_2-\eta_1)}{\eta_2} \tag{12}$$

If the discontinuity is a small fraction of the ambient viscosity, R_η will be close to zero. If the discontinuity $(\eta_2-\eta_1)$ is positive and large, R_η can approach unity. If there is a decrease in viscosity from zone 1 to zone 2, R_η will be negative.

We use the nondimensional discontinuity, R_η to further assess the performance of the densification relations. Figure 2.3 shows R_η over a range of climatic conditions. The black line represents one scenario of the Clausius-Clapeyron relationship. Like the estimated viscosity

shown in Figure 2.2, R_η values varies significantly among the models. The Herron and Langway (1980), Li and Zwally (2011), and Simonsen (2013) models show a variation in R_η between around -1 and 1. The Arthern et al. (2010), Kuipers Munneke (2015), and Ligtenberg et al. (2011) models show little variation in R_η comparatively.

For the Herron and Langway (1980) model, the largest R_η is at sites with high accumulation. The climate regime in the upper left of Figure 2.3 (high accumulation rate, low temperature) has not been observed on Earth, but conditions in the upper right (high accumulation rate, high temperature) are more common.

2.5 DISCUSSION

The viscosity in real-world firn is likely to vary at small (cm) scales due to differences in the microstructure. However, none of these common firn-densification relations attempt to simulate microstructural behavior; instead, they are based on similar empirical concepts and assumptions for estimating macroscopic behavior**.** Therefore, the sharp discontinuities at the zone 1-zone 2 boundary are a clear indicator of the limitations of such an empirical, macroscopic approach. In the following subsections, we further investigate the discontinuities to gain insight into the length scales of the shift in dominance between mechanisms responsible for firn densification.

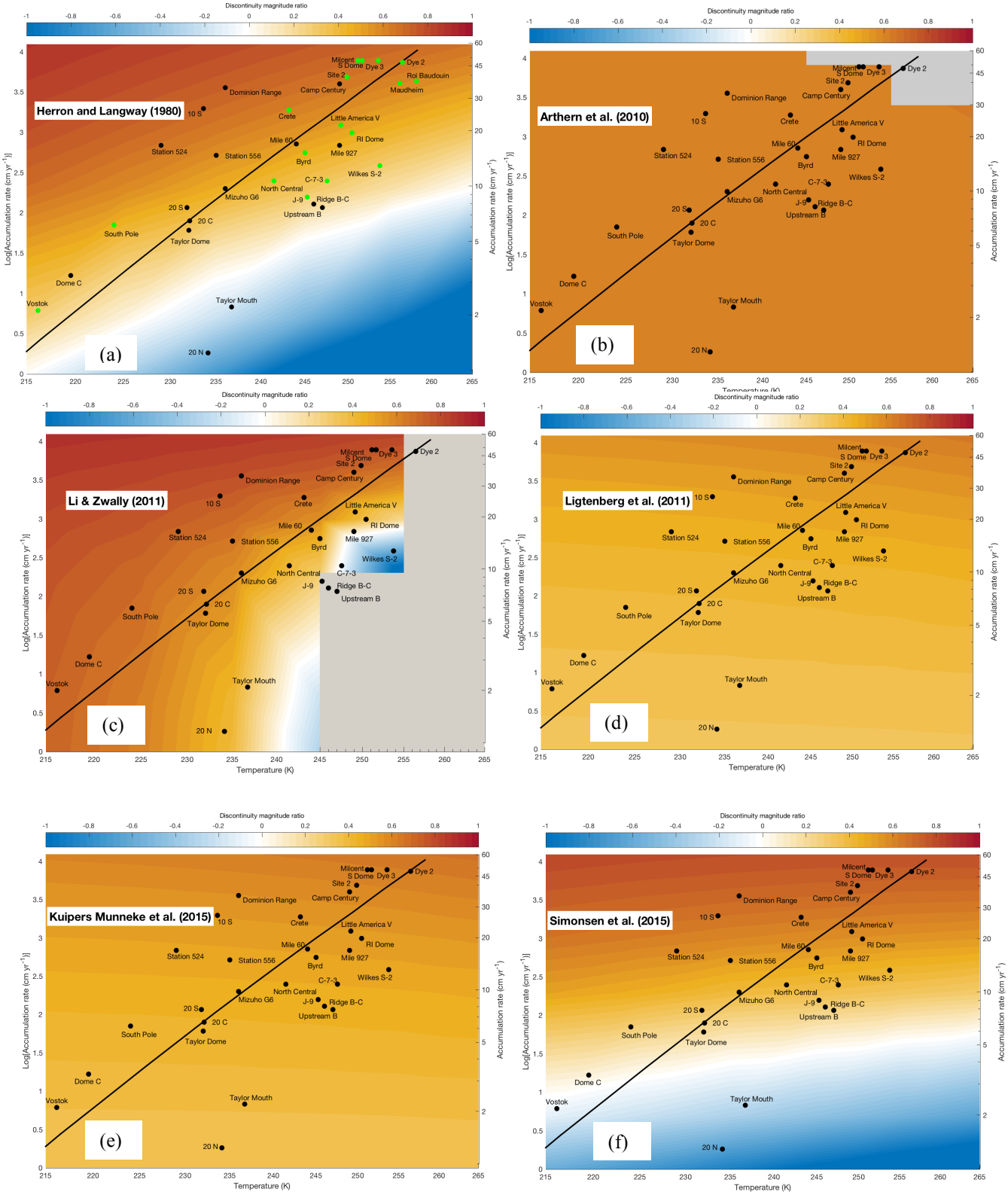

Figure 2.3. Climate maps for all models showing the nondimensional discontinuity R_η for the boundary between zone 1 and zone 2. Models include (a) Herron and Langway (1980), (b) Arthern et al. (2010), (c) Li and Zwally (2011), (d)Ligtenberg et al. (2011), (e) Kuipers Munneke et al. (2015), and Simonsen et al. (2015).

2.5.1 ANALYZING R_η FOR HERRON AND LANGWAY (1980)

Many firn-densification models are modified from the fundamental equations and assumptions of the Herron and Langway (1980) model, and so we focus our further discussions on this model. The model predicts a large range of R_η (Figure 2.3). This large range also occurs with the Li and Zwally (2011), and Simonsen (2013). In general, sites used in the Herron and Langway (1980) calibration (green dots) have smaller discontinuities and tend to lie close to the particular Clausius-Clapeyron curve shown in Figure 2.4. However, note that there is a deviation of slope between the Clausius-Clapeyron black line and the slope where R_η values are equal.

We can gain insight into the cause of the large discontinuities by rewriting Equation (12) with the equations for η_1 and η_2 (Equations (10) and (11)):

$$R_\eta = 1 - \left[\frac{k_2}{k_1}\exp\left(\frac{E_1 - E_2}{RT}\right)A^{-\frac{1}{2}}\right] \tag{13}$$

All variables in Equation (13) are constants except the accumulation rate *A* and temperature *T*. For R_η values to remain close to unity, *T* and *A* must covary, which is what we observe for many of the sites which lie along the Clausius-Clapeyron relationship. Although values of $R_\eta < 0$ are physically unrealistic, Equation (13) suggests that negative R_η values (e.g., Taylor Mouth, 20 N) occur when *A* is sufficiently small and *T* is sufficiently large so that the right-hand-side term approaches or exceeds unity. For R_η to be a large positive value (e.g., 10 S), *A* must be large and *T* must be small. To analyze such relationships quantitatively, we calculate the partial derivatives of R_η. First, when R_η varies with *A* at a constant temperature $T = T_0$, i.e. along a vertical slice through Figure 2.4, the partial derivative of R_η becomes Equation (14).

$$\frac{\partial R_\eta}{\partial A} = \frac{1}{2}\frac{k_2}{k_1}\exp\left(\frac{E_1 - E_2}{RT_0}\right)A^{-3/2} \tag{14}$$

Equation (14) is always positive so R_η will always increase with increasing accumulation rate A, which confirms the transition from blue to red color for every temperature vertical slice in Figure 2.4. When R_η varies with T at a constant accumulation rate $A = A_0$, i.e. along a horizontal slice through Figure 2.4, the partial derivative of R_η becomes Equation (15).

$$\frac{\partial R_\eta}{\partial T} = \left(\frac{k_2}{k_1} A_0^{-\frac{1}{2}}\right) \exp\left(\frac{E_1 - E_2}{RT}\right)\left(\frac{E_1 - E_2}{RT^2}\right) \tag{15}$$

All factors are positive except $(E_1 - E_2)$, so Equation (15) is always negative, which confirms the transition to bluer colors in Figure 2.4 toward higher temperatures along a horizontal slice at a constant accumulation rate.

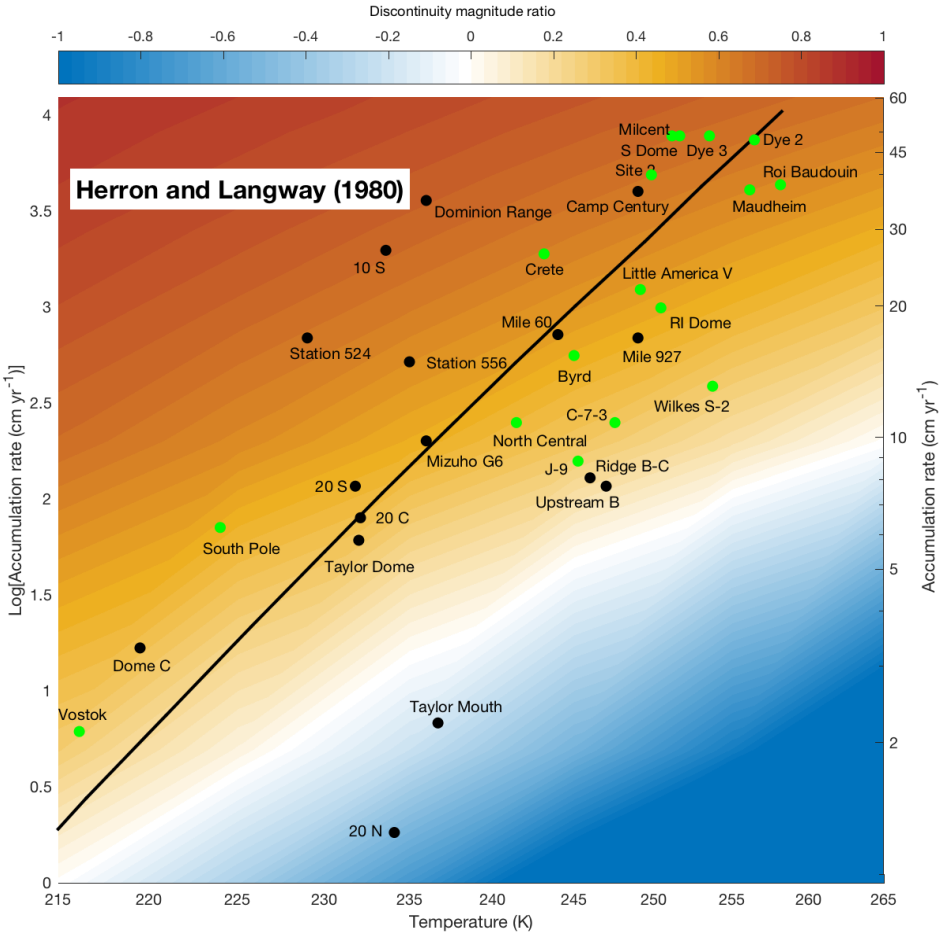

Figure 2.4. Herron and Langway discontinuity magnitude ratio with some calibration sites plotted in green dots.

2.5.2 DEFINING A TRANSITION ZONE

The viscosity discontinuity in many models at the zone 1-zone 2 boundary is due to the model formulation. The models' empirically-tuned parameters for each zone are based on measured depth-density profiles so that the equations simulate different dominant processes in each zone. Generally, those processes are thought to be grain settling/boundary sliding in zone 1, and grain sintering in zone 2. The discontinuities are a manifestation of the abrupt change in physical mechanisms assumed to occur at a density of 550 kg m^{-3}. To better understand the implications of these assumptions on length scales in the firn layer, we introduce a linear transition in the governing equations between the zone 1 and zone 2 of the Herron and Langway (1980) model.

Rather than assuming an abrupt transition from zone 1 to zone 2 at 550 kg m^{-3}, we define a transition zone over an adjustable density range from ρ_{TZ1} to ρ_{TZ2}. We assume that the dominant densification mechanism transitions gradually from grain-boundary sliding to sintering throughout this transition zone. We define α to be a linear function of density that ranges from 0 to 1 through the transition zone, and we define the densification rate $\frac{D\rho_{TZ}}{Dt}$ in the transition region, $\frac{D\rho_1}{Dt}$ as the densification rate for zone 1, and $\frac{D\rho_2}{Dt}$ as the densification rate for zone 2. We use $\frac{D\rho_1}{Dt}$ for densities less than the upper bound of the transition zone and $\frac{D\rho_2}{Dt}$ for densities greater than the lower bound.

$$\frac{D\rho_{TZ}(z)}{Dt} = \alpha\left(\frac{D\rho_1(z)}{Dt}\right) + [\alpha - 1]\left(\frac{D\rho_2(z)}{Dt}\right) \quad (16)$$

Using this formulation, we run the model, compare the depth-density profile to the data and the original Herron and Langway (1980) output, and adjust the transition bounds to produce the lowest Root Mean Square Error (RMSE) between the model outputs and observations. The

bounds vary depending on the site. When the upper bound is less than 550 kg m^{-3}, densification occurs less quickly at those densities because of the influence of $\frac{D\rho_2}{Dt}$; when the upper bound is greater than 550 kg m^{-3}, the densification occurs more quickly because of the influence of $\frac{D\rho_1}{Dt}$.

Figure 2.5 shows depth-density data with profiles predicted by the Herron and Langway (1980) linear mix transition model and the original Herron and Langway (1980) model. The shaded polygon along each profile represents estimations from the Herron and Langway (1980) model given a potential uncertainty in measured temperature ($\pm$2 K) and accumulation rate ($\pm$2 cm a^{-1}) at each site. We choose to compare chosen sites above, below, and on the Clausius-Clapeyron curve that we show in Figures 2.3 and 2.4. Table 2.2 shows the transition zone bounds for each site. Figure 2.5 shows the results for these three representative sites: a site that lies on our Clausius-Clapeyron curve (Mizuho G6), a site that lies above the curve (Dominion Range), and a site that lies below the curve (Ridge B-C).

The 4 sites that lie near the Clausius-Clapeyron curve, such as Mizuho G6, Byrd, Vostok, and Taylor Dome (1994 core), do not show much improvement through using the transition zone model. For these sites, a transition zone between 500 kg m^{-3} – 600 kg m^{-3} can decrease the RMS error marginally by ~5% or less.

The Dominion Range depth-density profile is poorly approximated by the original Herron and Langway (1980) model. We can fit the data by extending the transition zone from the conventional boundary of 550 kg m^{-3} down to 917 kg m^{-3}, meaning that there is no region of the firn layer that is best approximated by zone 2 densification from the Herron and Langway (1980) model. The RMS error is decreased by almost an order of magnitude; similarly, from Figure 2.6, the residual plot shows that the curve fit is improved by using the transition model.

At Ridge B-C and Upstream B, which are warm, low-accumulation sites, show a decrease in RMS error for the transition zone model but the overall fit is not significantly improved. For Upstream B, the densification in zone 1 occurs more quickly than the rate defined by Herron and Langway, so neither model accurately estimates the depth-density data. For Ridge B-C, the densification occurs more slowly in zone 2 than the rate defined by the original Herron and Langway model, so neither model fits the depth-density data well (see Figure 2.5). The transition

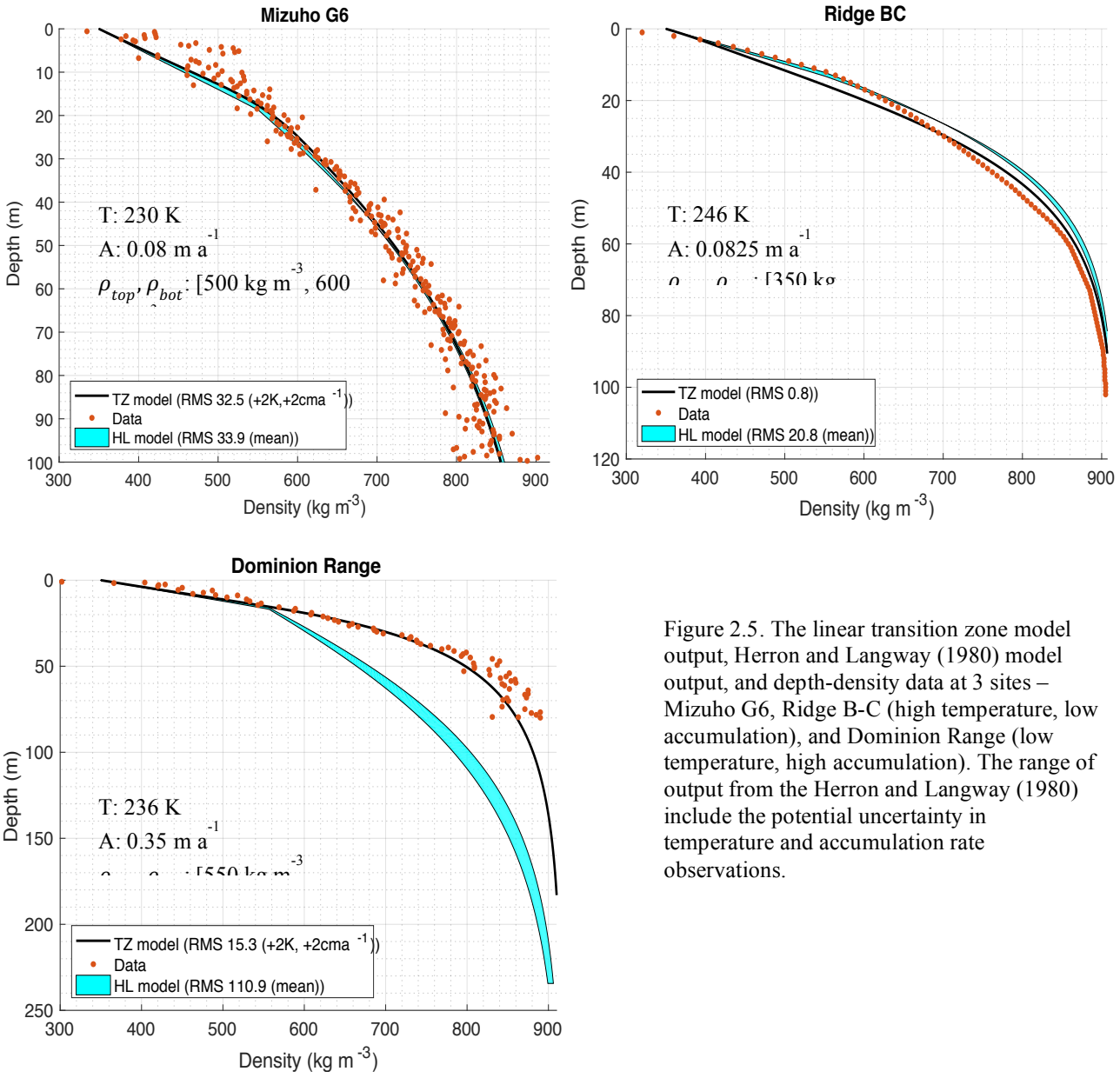

Figure 2.5. The linear transition zone model output, Herron and Langway (1980) model output, and depth-density data at 3 sites – Mizuho G6, Ridge B-C (high temperature, low accumulation), and Dominion Range (low temperature, high accumulation). The range of output from the Herron and Langway (1980) include the potential uncertainty in temperature and accumulation rate observations.

model reduces the RMS error at Ridge B-C but improves the fit only in zone 2 and actually reduces the fit in zone 1. This is best visualized through select residual plots in Figure 2.6. The Ridge B-C residual plot indicates a tradeoff between accuracy in zone 1 and zone 2 but not an overall substantial improvement of the curve fit.

Table 2. The transition zone bounds for the 9 sites and associated climatic conditions.

Site Name	Upper bounds (ρ_{top})	Lower bound (ρ_{bot})	T, A
Byrd	500 kg m^{-3}	600 kg m^{-3}	245 K, 15.6 cm a^{-1}
Dominion Range	550 kg m^{-3}	917 kg m^{-3}	236 K, 15.6 cm a^{-1}
Dye 3	450 kg m^{-3}	550 kg m^{-3}	255 K, 50 cm a^{-1}
Mizuho G6	450 kg m^{-3}	550 kg m^{-3}	230 K, 0.08 cm a^{-1}
Ridge BC	350 kg m^{-3}	550 kg m^{-3}	246 K, 0.0825 cm a^{-1}
South Pole	400 kg m^{-3}	450 kg m^{-3}	224 K, 0.0637 cm a^{-1}
Taylor Dome	500 kg m^{-3}	600 kg m^{-3}	232 K, 0.0596 cm a^{-1}
Upstream B	350 kg m^{-3}	360 kg m^{-3}	247 K, 0.079 cm a^{-1}
Vostok	600 kg m^{-3}	700 kg m^{-3}	232 K, 0.022 cm a^{-1}

These results suggest that the Herron and Langway (1980) model is characterizing densification processes for zone 1 and 2 inaccurately and, in few cases, some processes or factors may be missing. For example, the Dominion Range site is located in a localized accumulation basin in the Transantarctic mountains at the confluence of the Beardmore and Mill Glaciers, and is subject to strong katabatic winds, and so is a cold, high-accumulation site. (Mayewski et al.,1995; Mayewski et al.,1990). The very wide transition zone used in the transition model

indicates that the fit to the data is improved if zone 1 behavior dominates up to ice density, and suggests the length scale over which zone 1 versus zone 2 processes occur is not captured by the original Herron and Langway (1980) model. The Herron and Langway (1980) model is empirical and does not assign individual processes to zone 1; instead, processes in zone 1 are simply assumed to occur faster than in zone 2. Such empirical constructions may not be able to completely separate the influence of temperature and overburden load on densification processes or microstructural changes caused by other factors (e.g., wind). Thus, we cannot resolve which processes are more active to greater depths from the available data and model output. However, we do know that loading occurs relatively quickly at the Dominion Range site, so processes that are driven by overburden pressure may occur more quickly compared to those that are driven by temperature. Additionally, microstructure properties of the firn may allow the length scales to which densification processes are active to change. For example, Alley et al. (1982) observed faster densification in coarser-grained firn compared to finer-grained firn and attributed this finding to how firn structures respond to loading. In coarse-grained firn, near-surface vertical vapor or heat transport produce crystals with vertical shape orientations, creating a grain arrangement that is below maximum closest packing. Thus, the grain can be influenced more readily by particle rearrangement driven by overburden loading (Alley et al., 1982). In contrast, fine-grained firn crystals, generally caused by wind-packing and large, near-surface temperature gradients, tend to be more spherical and joined by smaller necks to more neighbors (Alley et al., 1982). Thus, the grain arrangement is close to maximum packing and may be more stable under overburden loading because particles are less capable of rearrangement, producing slower densification in response to the same load and temperature (Alley et al., 1982).

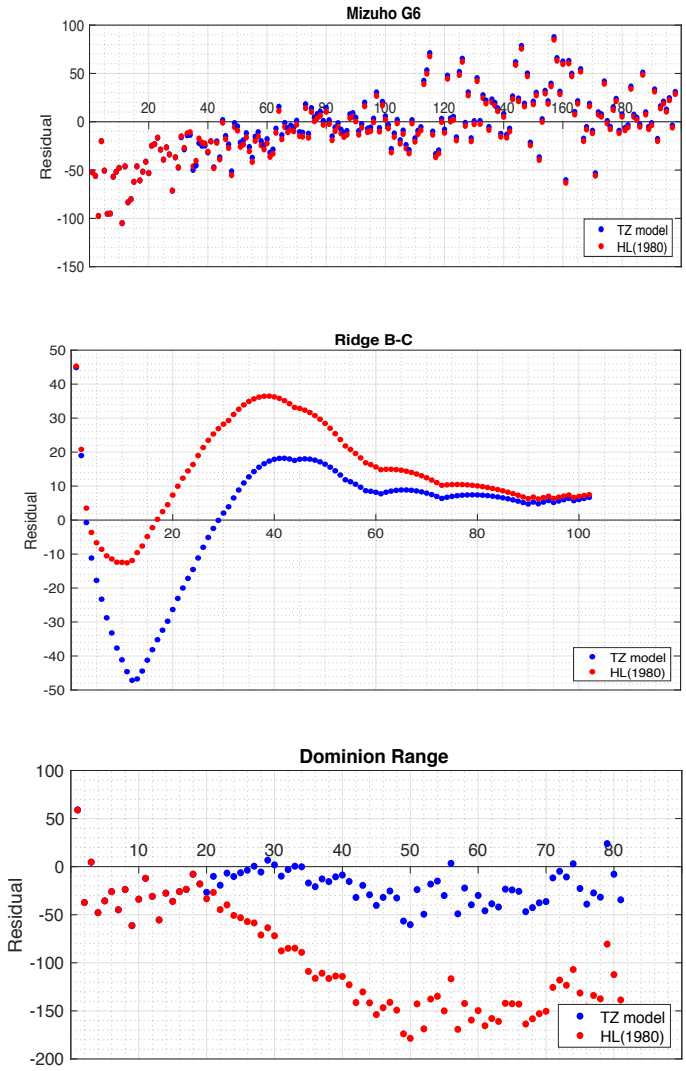

Figure 2.6. The residuals for Mizuho G6, Ridge B-C, and Dominion Range site.

For Ridge B-C, a warm, low-accumulation site, the upper firn densifies according to the zone 1 rate, but the lower firn densifies much slower than the zone 2 rate. The slow densification rate suggests that zone 2 processes driven by the overburden load (e.g., sintering) occur slower than at other sites due to the low accumulation rate at Ridge B-C, and that the Herron and Langway (1980) model may not capture the distinct influence of overburden load versus temperature on such processes. Additionally, Ridge B-C, influenced by ice stream dynamics, may be affected by shearing dynamics and the dominance of different densification processes (Conway et al., 2002).

2.6 CONCLUSION

Most commonly used firn-densification models are empirically-based and tend to describe macroscale behavior without consideration of microscale effects. These models also divide the firn layer into two unique regions – zone 1 (surface density to 550 kg m^{-3}) and zone 2 (550 kg m^{-3} to ice density) – and so their densification rate equations change across the boundary of 550 kg m^{-3}. The models predict continuous depth-density profiles at this boundary, but their distinct zone 1 and zone 2 densification equations cause the implicit firn viscosities to have unrealistic discontinuities. This suggests that these models are not accurately characterizing fundamental processes important to firn densification into their macroscopic, empirically-based description. Viscosity differences are directly related (through a viscous constitutive relation) to fractional strain-rate differences, so these viscosities must be normalized to compare viscosity discontinuities at different sites. The largest normalized values occur at higher temperature, high accumulation sites and those that do not follow regular, Clausius-Clapeyron pairs of temperature and accumulation rate. In some instances, a negative discontinuity is seen, which signifies a decrease in viscosity with depth. This suggests that the current model framework is specifically representing underlying physics of densification at the transition inaccurately. To address the viscosity discontinuity issue, we created a model that transitions linearly from the Herron and Langway (1980) zone 1 to zone 2 densification rates through a zone near the traditional 550 kg m^{-3} critical density. We found that the boundaries for the transition zone varied by site. When we match the model output to depth-density data, we see that the range of the transition zone must be around 100-200 kg m^{-3} and the transition zone bounds are site-dependent. Some sites, however, are unique; Dominion Range requires the transition zone to be extended to ice density, and even though the transition zone model reduces the RMSE for Ridge-BC, there is a tradeoff

between the fit for zone 1 and zone 2. Such results suggest that there is a distinct influence of temperature and overburden pressure on densification processes, and that other factors, such as shearing or wind, are also important. They also suggest that modifying empirically-constructed firn-densification models (e.g., the Herron and Langway (1980)) will only go so far to improve densification rate estimates, and we recognize the need for a model framework based on microphysics or microstructural evolution.

Chapter 3. USING THE EVOLUTION OF MICROSTRUCTURES FROM MICRO-CT DATA TO MODEL FIRN DENSIFICATION

3.1 ABSTRACT

We have a poor understanding of how existing firn-densification models perform when applied outside their climate calibration range, and during climate transients. Firn-densification models are important for several applications, including estimating ice-sheet mass loss estimates from repeat satellite altimetry, and uncertainties in firn-densification rates from such models are among the largest for this method. These models are empirically constructed for estimating the macroscopic behavior of the firn layer; they are not built to simulate microstructural behavior. No relation so far exists that is either fully physically-based or is applicable to the entire firn column. Here we construct a model by modifying a relationship introduced by previous work to estimate densification in the upper firn layer through the transition region. The model is based on both grain-boundary sliding and sintering. The framework is developed so that the densification rate is related to viscosity through a standard constitutive equation, and so that viscosity is based on microstructural evolution. We analyze the USP50 micro-CT dataset to define the evolution of three key microstructural parameters (average object area-equivalent circle diameter, neck size, and coordination number) and compare these descriptions to several prominent historical studies. We model the upper firn layer (4 m to 47 m) at USP50 and at other sites (e.g., Dome C, Vostok) and find good agreement between the model and data. This work provides a key step in producing a firn-densification model based on microstructural evolution. However, more work is necessary for advancing the model, including collecting more data to constrain microstructural evolution in a range of climatic conditions.

3.2 INTRODUCTION

Our knowledge of grain-scale processes comes from research predominantly from the 1950s-1980s, and their interactions and roles in firn densification are still incompletely understood (e.g., Wilkinson and Ashby, 1988; Alley, 1987; Arthern and Wingham, 1998; Lundin et al., 2017). Because of this, firn-densification models are empirical or semi-empirical, and are mainly calibrated against measured depth-density profiles using local climate to define key model parameters. These are phenomenological models, and so strive to simulate behavior on the macroscopic level from specific loading and thermal conditions but do not explicitly include processes or evolution occurring on the microscale (Cresseri, 2005; Cresseri and Jommi, 2005). We do not have a clear understanding of how firn-densification models behave when they are applied 1) outside their climate calibration range, and 2) during climate transients (Lundin et al., 2017). Data used to calibrate models span a limited range of climatic conditions even when the data are not regionally restricted.

Most models assume steady state by tuning compaction rates to modern depth-density profiles, which are considered to be in steady-state (e.g., Herron and Langway, 1980). The commonly used firn-densification models are based on the suggestion of Robin (1958), i.e., that each fractional decrease in porosity is proportional to an incremental increase in overburden load, which is inherently a steady-state assumption. These limitations in model construction can contribute to error in model predictions when these firn-densification models are applied over a wide range of climates and are used to describe transient firn. Several models (e.g., Arthern et al., 2010) estimate the evolution of firn density by using in-situ measurements of firn compaction and/or deriving a semi-empirical relation based on the evolution of one or a few types of microstructures. However, a firn-densification model that is 1) widely applicable and accurate

for the spatial and temporal range of climate regimes on the ice sheets and 2) has been demonstrated to reliably simulate densification during transient climate does not yet exist.

Improving the quality of firn-densification models will be important for yielding reliable estimations of mass loss across both Antarctica and Greenland. Phenomenological models will only go so far in accurately approximating firn densification. Thus, we aim at to derive a micromechanical model, i.e. a model that considers microstructural influence in deformational processes, for the evolution of firn (Cresseri, 2005; Cresseri and Jommi, 2005). One challenge in using micromechanical models to describe macroscopic behavior is how to link microscale evolution to macroscale evolution. In this chapter, we develop a model that serves as a first step in creating such a model by using the evolution of microstructures to characterize firn densification in the upper and transition zone (around 550 kg m^{-3}) of the firn layer. Previous studies have described densification with an abrupt transition between dominant processes (e.g., grain-boundary sliding and sintering) at 550 kg m^{-3}. In contrast, we aim to describe densification in a transition zone using a combination of processes without an abrupt transition. The model is an extension of the model by Feldt and Ballard (1966), and evolution equations for microstructures are inferred from micro-CT data from a firn core from USP50 near South Pole. We then apply this model to sites with other climate conditions.

3.3 DERIVING A MODEL BASED ON MICROSTRUCTURAL EVOLUTION

3.3.1 FRAMEWORK THAT BYPASSES THE ROBIN HYPOTHESIS

The model framework is outlined in Figure 3.1 and follows a Lagrangian approach. Letting ***s*** represent a vector of microstructural parameters, then during each time step, the model solves: microstructural evolution ($D\boldsymbol{s}/Dt$); a viscosity equation that is dependent on the microstructural state (***s***) at time t; and densification rate $D\rho/Dt$ of each firn parcel using a constitutive relation connecting strain rate to stress through viscosity.

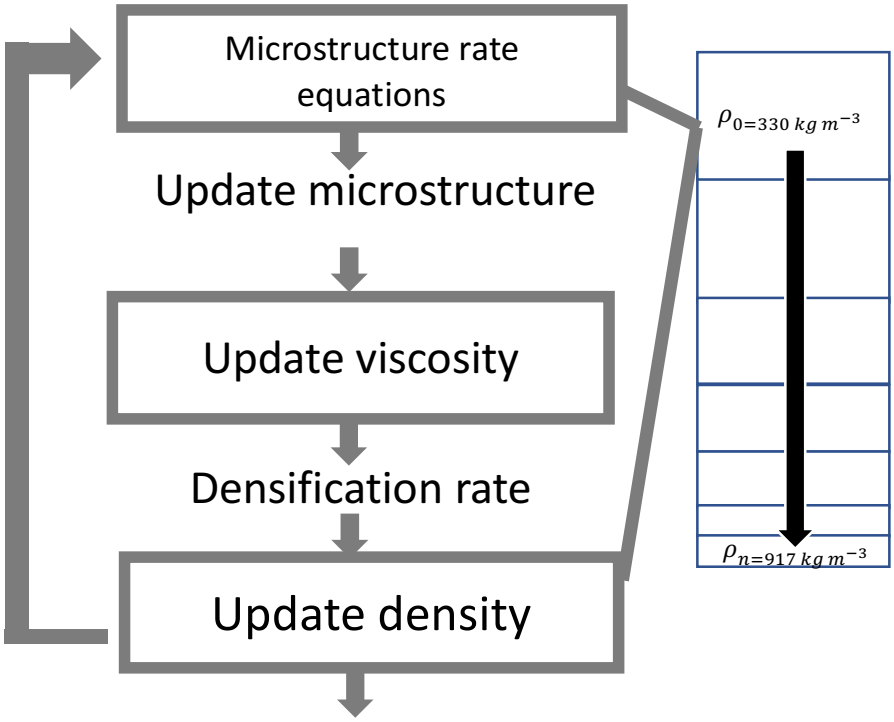

Figure 3.1. The Lagrangian framework of the model.

Past work has shown that the effective viscosity is controlled by and can significantly change due to a change in ice temperature, presence of impurities, crystal orientation, liquid water content, and microstructural parameters (e.g., coordination number, bond radius, and

crystal/grain size) (e.g., Brown et al., 2001). For example, microstructural properties of the snow layer may have a "softening" or "hardening" effect (which can also be applied to the firn layer), acting to weaken or stiffen the firn, which may not have been indicated simply by using its density. Therefore, we can construct a relation for $\frac{D\rho}{Dt}$ that bypasses Robin's suggestion and that is instead dependent the influence of evolution of microstructures on firn viscosity

$$\frac{D\rho}{Dt} = -\frac{\rho\sigma}{2\eta\,(\rho,\boldsymbol{s})} \tag{1}$$

where σ is the overburden stress and $\eta\,(\rho, \boldsymbol{s})$ is the firn viscosity dependent on the current density and microstructural state. The evolution of microstructural parameters $\boldsymbol{s}$ is controlled by mechanisms such as vapor transport; surface, lattice, and boundary diffusion; and Coble and Nabarro-Herring diffusional creep (Maeno and Ebinuma, 1983). Their rate equations represent the structural transformations caused by the ensemble of these mechanisms.

To define the dependence of viscosity η on the microstructural state *s*, we modify a relationship introduced by Feldt and Ballard (1966). Feldt and Ballard (1966) developed a theory for the consolidation of age-hardened 'snow' under uniaxial stress. Their theory is applicable only for densities between ~410 – 600 kg m^{-3} because it is based on physics of grain-boundary sliding, which occurs mainly in the upper firn (see Alley, 1987). In particular, the theory stems from considering a confined cylindrical snow mass with a specified overburden load. The shear stress induced from the overburden load on the grain bonds produces intergranular slide accommodated by viscous flow of the ice in these bonds, which leads to the eventual increase in density (decrease in porosity). This is applicable to lower density firn because densification beyond 600 kg m^{-3} is thought to occur by sintering or, according to Feldt and Ballard (1966), the 'mutual intrusion of the particles'.

Here, we extend the Feldt and Ballard (1966) theory to build a model that represents the upper firn into and through the transition zone. In section 3.22, we describe the theory from Feldt and Ballard and my modifications to it.

3.3.2 THEORY

A parcel of firn is composed of grains connected by k bonds, and the volume of the pores, V_v, is composed of k volume elements with a 'common dimension', r. The volume element is expressed as Equation 2, where α is a volume shape factor.

$$\frac{V_v}{k} = \alpha r^3 \tag{2}$$

Small shear strains, $\delta\epsilon_i$, occurring in the bonds, reduce V_v by δV_v, while pore volume changes geometry according to k geometrical parameters λ_i, where

$$-\delta V_v = \sum_{i=1}^{k} \alpha r^3 \lambda_i \delta\epsilon_i \tag{3}$$

The fractional change in pore volume can be approximated by using both Equations 2 and 3.

$$\frac{-\delta V_v}{V_v} = \frac{1}{k}\sum_{i=1}^{k} \lambda_i \delta\epsilon_i \tag{4}$$

Sliding along the grain boundaries induced by shearing stresses causes the parcel of firn to be 'less resistant to flow' (low viscosity) than the parcel of firn with no grain-boundary sliding because it weakens the structure of the firn. However, at some depth, other factors begin to dominate – the growth of grains and the increase in bonding (coordination number) and neck size strengthen the firn and cause the parcel of firn to become 'more resistant to flow' (higher viscosity). This sintering process essentially can be thought of interwoven microstructural changes, where the initial contact point between two grains increases in size and grain growth occurs, the latter especially in the intermediate stage of sintering (German, 1996). Thus, a grain once in the upper firn will eventually become too constrained to slide past its neighbors because

of the development of a neck, grain growth of neighboring grains, and the increase in coordination number of grains in close proximity. Initially, the shearing stresses τ_i in the grain bonds cause strains $\delta\epsilon_i$ in time δt

$$\delta\epsilon_i = \frac{\tau_i\, \delta t}{\eta_{ice}} \tag{5}$$

which is dominated solely by shearing associated with grain-boundary sliding. However, when the grain neck and grain growth become initiated, τ_i ideally becomes smaller as grain-boundary sliding slows and sintering ultimately takes over densification. To define τ_i, we can define *P* as the axial force and *S* as a surface which intersects only grain bonds in the planes of τ_i (which are usually perpendicular to *P*), the number of bonds intersected by *S* as *l*, the area of each cross-section of a bond is A_i, the angle between the normal to A_i and the direction of *P* as θ, and the vertical force on A_i as $\frac{PAcos\theta}{\sum_{i=1}^{k} A_i cos\theta}$. We can also evolve A_i as the cross-sectional area grows, $A_i(t)$. However, this description could only be applied to early and early-intermediate stage sintering where the initial growth of the bonds occurs and there is the decrease of shearing associated with sliding from the growth of this bond area. In reality, the tension, shear, and compression stress distribution in the contact region is complex (German, 1996). Instead of providing a detailed theoretical guess as to how we can define this influence, we define a simple factor *c* that aims at describing the decrease in τ_i from the counteraction of the growth of grains. This factor *c* aims to be a simple representation of the influence of grain growth with respect to bond growth that resists sliding, reducing the shear stress in the bond area. We define $c = \frac{\Delta \mathrm{r(t)} \cdot \mathrm{b}}{\Delta A_i(t)}$, $\tau_s = \frac{Pcos\theta sin\theta}{\sum_{i=1}^{l} A_i(t) cos\theta}$, where Δr and ΔA_i is the difference between the grain radius and bond area between one timestep, respectively, and *b* is a constant. Then, the expression for τ_i becomes

$$\tau_i = \tau_s / c\ . \tag{6}$$

To derive an expression for viscosity η, we follow the approach by Feldt and Ballard (1966) by first substituting Equation (5) into Equation (4), which produces

$$\frac{-\delta V_v}{V_v} = \frac{\delta t}{k\eta_{ice}} \sum_{i=1}^{k} \lambda_i \delta \tau_i. \tag{7}$$

If the 2-D porosity of the surface *S* projected on a plane perpendicular to *P* is identical with the effective porosity, n_f of a potential failure surface (see Ballard and McGraw (1965)), and *A* is the cross-sectional area of the mass, then

$$n_f = \frac{A - \sum_{i=1}^{l} A_i cos\theta}{A} \tag{8}$$

$$\tau_i = \frac{\sigma cos\theta sin\theta}{c(1-n_f)} \tag{9}$$

where σ represents *P/A,* axial external stress. If equation (9) is combined with Equation (7) and if we assume that δt approaches zero and $\frac{1}{V}\frac{dV}{dt} = \frac{1}{z}\frac{dz}{dt}$, then

$$\frac{-dV_v}{V_v dt} = \frac{\sigma}{ck\eta_{ice}\left(1 - \frac{A - \sum_{i=1}^{l} A_i cos\theta}{A}\right)} \sum_{i=1}^{k} \lambda_i cos\theta sin\theta \tag{10}$$

where volume of the pores, V_v, the area of each cross-section of a bond is A_i, the pore volume changes geometry according to *k* geometrical parameters λ_i, the number of bonds intersected by a surface *S* which intersects only grain bonds in the planes of τ_i is *l*, and the angle between the normal to A_i and the direction of the axial force *P* is θ.

As a starting point, we make several assumptions. First, we assume θ to be 180° for simplicity; however, we note that the invariance of this quantity is not confirmed *(*Feldt and Ballard*,* 1966), but considerably more research would be needed to derive appropriate values for the variation in θ. Additionally, Feldt and Ballard (1966) state the physical significance of the property λ_i is not readily pictured; however, if the pore space geometry remains similar, then it can be assumed that λ_i is independent of the porosity. Feldt and Ballard (1966) replace the

quantity $\frac{1}{k}\sum_{i=1}^{k}\lambda_i \sin\theta\cos\theta$ by a constant to describe their age-hardened snow and we assume similarly, for simplicity, that the value λ_i remains unchanged and can be written as a constant v_s. We combine v_s with b and $\Delta A_i(t)$in a constant v. Then, we can write the expression for viscosity as

$$\eta(t) = \frac{\eta_{ice}}{v}\frac{k(t)\sum_{i=1}^{l}A_i(t)\Delta r(t)}{A(t)}\,. \tag{11}$$

To solve Equation (11), we must define the evolution of microstructural parameters (bond area, number of bond connections, and grain size). Our goal is to use this model to estimate firn densification over a wide range of climatic conditions, but this requires knowledge and data of microstructural evolution $(k(t), A_i(t), r(t))$ in these climatic conditions. Thus, we explore the capabilities of our model using a micro-CT dataset from USP50m, a site 50 km from South Pole, to derive microstructural evolution equations $(k(t), A_i(t), R(t))$ for Equation (11). We also compare these microstructural descriptions to several prominent historical studies.

3.4 MICRO-CT DATA FROM USP50

The micro-CT dataset is from a 120-m firn core that was retrieved from USP50. The core was cut into 10-cm sections and processed for density, permeability, and micro-CT data at Dartmouth College and CRREL. Nearly continuous data exist from the surface down to 47 m, and 109 m to 114 m. The micro-CT data were recovered by the Bruker Micro CT Analyser using an image size of 1071, a resolution of 70.29μm, thresholding of 62 for lower grey and 255 for upper grey, and despeckling. Thresholding is performed before the analyses.

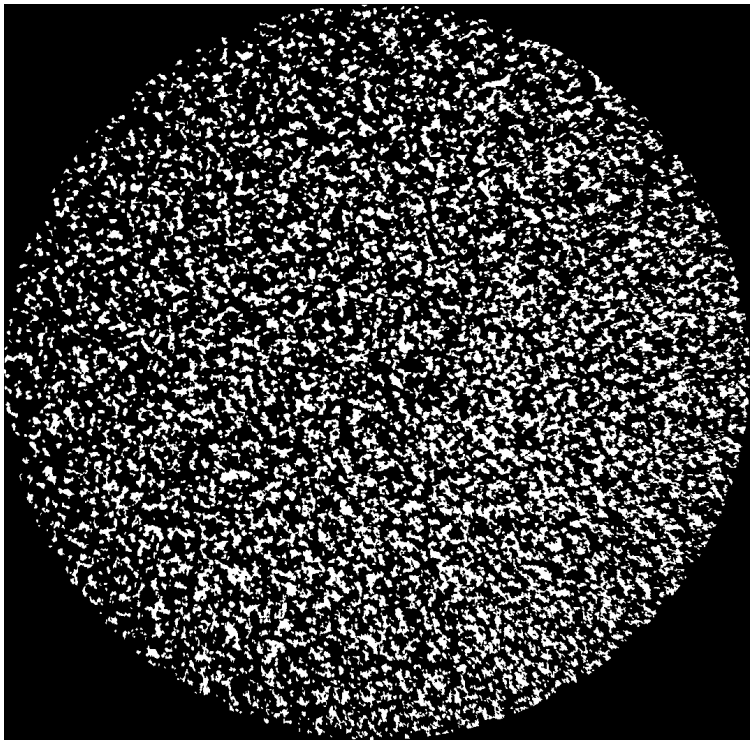

Figure 3.2. A binarized image showing the cross-section of the USP50 firn core at 4 m depth.

Several types of analyses are done by the CT analyzer. 3-D morphometric analyses find parameters in 3-D space using a surface-rendered volume model, and 2-D morphometric analyses find parameters in 2-D space using binary cross-sectional images (Bruker-MicroCT). Integrated and individual analyses can be performed in both 3-D and 2-D. In integrated analyses, parameters are determined when objects in a region are collectively analyzed and the total or mean value is given. In individual analyses, parameters for discrete objects are determined from connected voxels or pixels and the value is given for each object in the region (Bruker-MicroCT). Parameters are calculated from a selected region or volume of interest. A region of interest (ROI) is defined as the selection from a cross-sectional image, whereas a volume of interest (VOI) is defined the sum of ROIs from adjoining cross-sectional images (Bruker-MicroCT). Generally, 2-D analyses are done on ROIs and 3-D morphometric analyses are done

on VOIs. However, slice-by-slice analysis, for example, can be performed when a 2-D analysis is done on a VOI and works by integrating or summing the results over sets of images (Bruker-MicroCT). The consistency of selection is essential for the data quality (Bruker-MicroCT, 2019). For example, edge effects from handling and cutting the cores can adversely influence the data but can be properly managed by selecting a smaller central region or volume of interest.

Naming of the parameters from the analyses is based on either the "General Scientific" or "Bone ASBMR" system (Bruker-MicroCT). The Bone ASBMR names are derived from a symbol classification for bone histomorphometry (Parfitt et al., 1987).

Binarized images are produced using thresholding with lower grey and upper grey limits of 62 and 255, respectively. Subsequently, despeckling the images must be done to remove white and black specks or less than 4 pixels, which are secondary effects from thresholding. Figure 3.2 shows a binarized image after the thresholding and despeckling process has been performed.

3.5 EVOLUTION OF MICROSTRUCTURE PARAMETERS

To reconcile the terminology used in the Feldt and Ballard (1966) model expansion and the micro-CT data, the following definitions and assumptions are used. From the literature, a grain bond is the minimum constriction between two grains in the neck area, whereas the neck is defined as the total constriction (Eden and Brown, 1991). Characterizing a neck versus bond is seen in Eden and Brown (1991) diagram (Figure 3.3); these definitions can be subjective and the former can be difficult to apply in many cases. Thus, we define the number of bonds to be the number of necks defined in a micro-CT cross-sectional binary image. As Eden and Brown (1991) also state, the coordination number is defined as the number of bonds per grain; we define this aptly as the connections per grain in Section 3.42. Lastly, we define the average object area-

equivalent circle radius (calculated from the average object equivalent circle diameter) as the grain radius in our model equations.

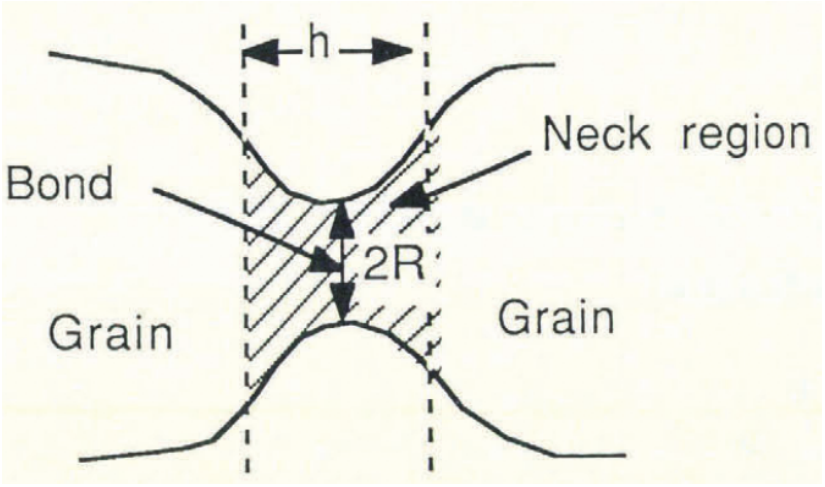

Figure 3.3. The definition of a bond versus a neck according to the figure 2 of Eden and Brown (1991).

3.5.1 AVERAGE OBJECT AREA-EQUIVALENT CIRCLE DIAMETER

Average object area-equivalent diameter is calculated from discrete objects in 2-D for each cross-sectional image and is the diameter of a circle with an equivalent area as the object (Bruker-MicroCT). Figure 3.4 shows this parameter for 11 samples of the USP50 core from around 29 m to 30 m deep to illustrate that there is considerable spread and variation even within a 10-cm core and across the entire 1 m. However, for simplicity, we use the mean value per 10-cm core for our subsequent work. We identify a simple evolution pattern of the parameter with depth by using a least-squares approach to calculate a best-fit line, as shown in Figure 3.5.

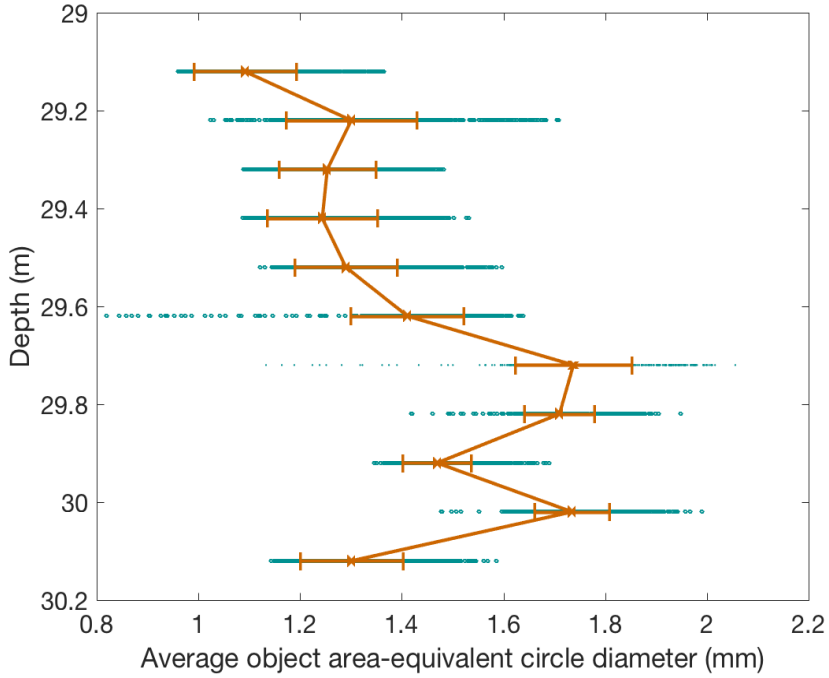

Figure 3.4. Average object area-equivalent circle diameter for 11 10-cm cores from around 29 m – 30 m deep. The teal circles represent the average object area-equivalent diameter for each object in the core; the orange bars represent the standard deviation for each core, and the solid orange line represents the variation with depth of mean average object equivalent circle diameter within the depth range.

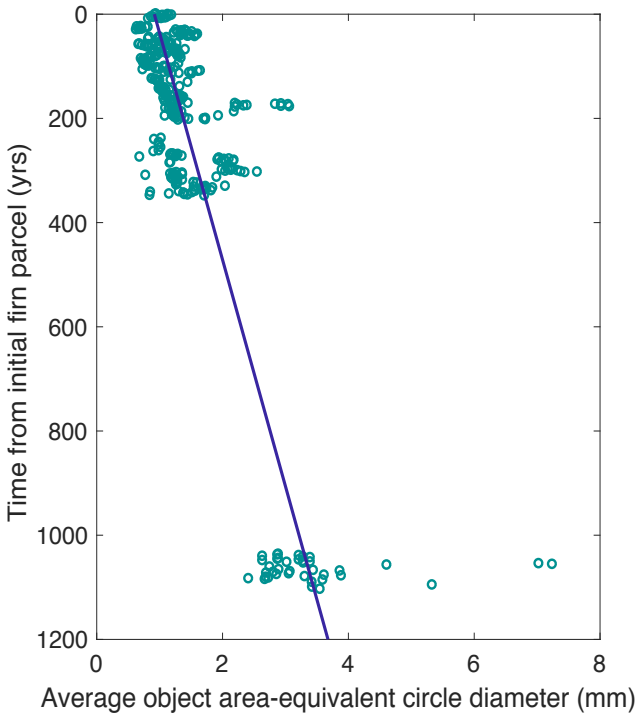

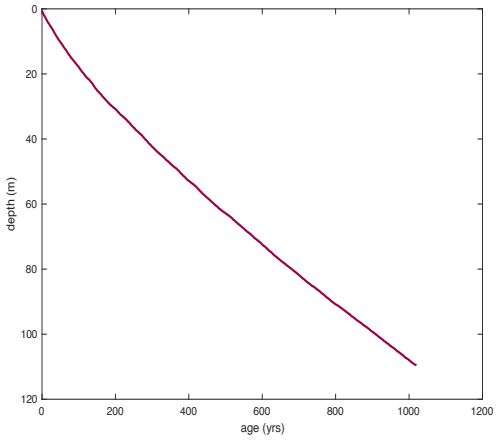

Figure 3.5. (Left) The estimated evolution of average area-equivalent circle diameter over time in the firn core using the depth-age timescale for the South Pole firn core (above).

A more useful relation for our model is one that identifies the evolution of the average object area-equivalent circle diameter over time. However, this requires the use of the assumption that each data point represents a single grain at different points in its evolution through the firn layer rather than many grains in their current state. Given the limitations of repeat collections and analysis of such types of data, this is a valid first assumption. To convert from depth to age, a timescale was calculated for the USP50 core from annual layer counting of both Na and Mg ion concentration by Dominic Winski of the University of Maine (see Figure 5). Figure 3.5 also shows the approximated average object area-equivalent circle diameter evolution through time using this depth-age scale.

We compare these results to those from Gow (1969), who studied the size of firn crystals and grains at South Pole using thin-sections and formulated an expression that predicts grain growth in the firn layer. This was later adapted for use in the Arthern et al. (2010) firn-densification model. Although the Arthern et al. (2010) model is commonly used to estimate densification for the entire firn layer, the grain growth formulation is technically applicable only to the upper firn. The South Pole firn crystal sizes that Gow (1969) analyzed ranged from approximately 0.24 mm^2 at 0.1 m to around 0.8 mm^2 at 48 m (but an average of 0.63 mm^2 at 49 m) (see figure 2 of Gow (1969)). Because these values are for crystals and not grains, we adjust the description for a valid comparison. From Gow (1969), grains and crystals show similar growth ratios in the beginning of recrystallization, and grains consist of only one or two crystals. The relationship between grain and crystal size at South Pole is described in table II of Gow (1969). We take the mean ratio between mean grain size and mean crystal size, 1.4, to convert the values given by the crystal growth rate at South Pole that Gow (1969) described. We then use the mean of the 10-cm cores as a comparison; the median produces similar results but with

slightly more spread. Although there is much variation in the USP50 micro-CT data, we can still make general comparisons to Gow (1969); Figure 6 compares these two grain growth formulations for the South Pole area. There is considerable deviation between the two formulations, which is most obvious below ~50 m (~400 years) in the firn layer. Gow's (1969) grain growth formulation only used data to a depth of 49 m at South Pole, but is a reasonable approximation for depths below 49 m (see inset of Figure 6). Even though the data from 109 m to 114 m are sparse and there is considerable spread, our results suggest that modelers should use the Gow (1969) formulation carefully below the data endpoints.

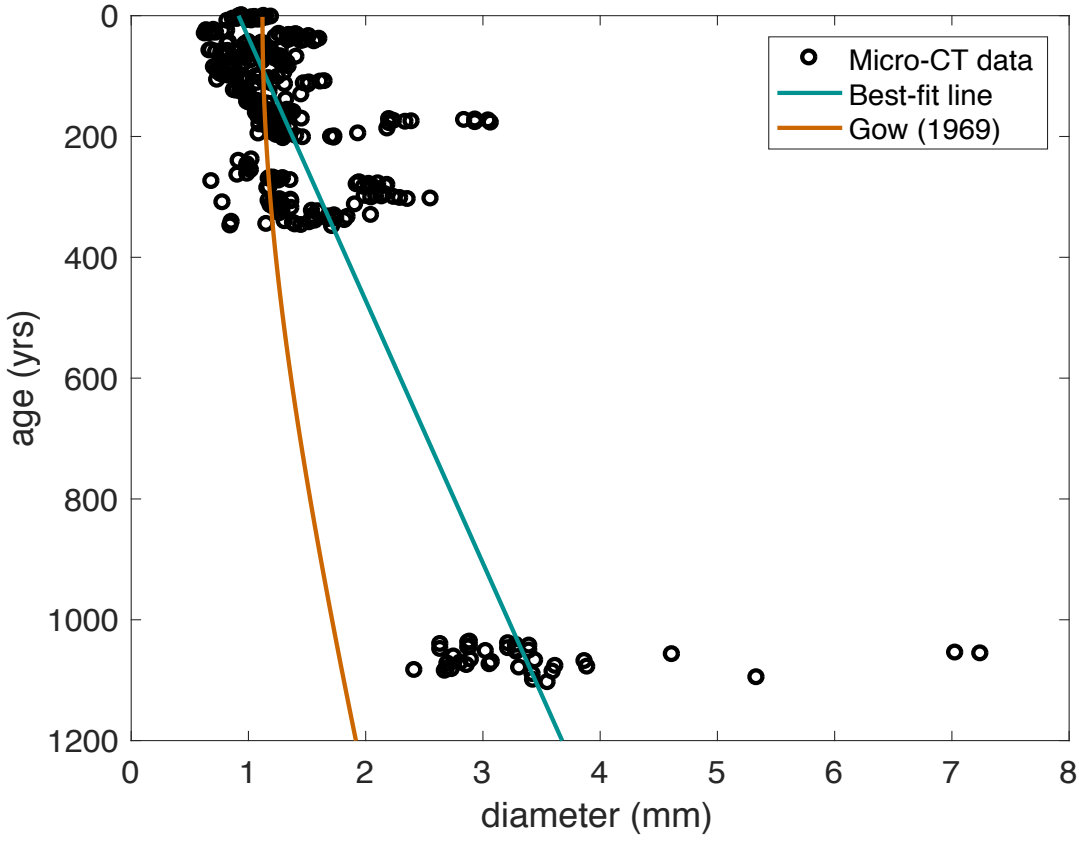

Figure 3.6. Comparison of the grain growth formulation of Gow (1969) and this work for the South Pole region.

3.5.2 CONNECTIVITY AND COORDINATION NUMBER

Coordination number of snow and firn describes the number of nearest neighbors to a grain. According to previous researchers such as Golubev and Frolov (1988), the coordination number evolves with density – the higher the coordination number, the higher the density. The maximum number of neighbors for a grain is directly related to the type of packing and material properties. For tetrahedral packing, the maximum coordination number is 4; during friable cubic packing, the maximum is 6. When the packing is most dense, the coordination number is 12 (Golubev and Frolov, 1998). Experimental data show that the relationship between density and the coordination number changes according to different values for the rigidity and structural friability parameters (Golubev and Frolov, 1998).

To calculate the coordination number, we use the connection density and the average volume of the grain per core to calculate the number of connections per grain. Due to errors in the 2-D and 3-D analysis for certain cores, we only analyze a depth range from 5 m to 30 m. Golubev and Frolov (1998) assume grains are spheres, so the average grain volume is calculated using the average object area-equivalent diameter, (Figure 3.7a). The comparison of the dataset, its best-fit line, and the Golubev and Frolov (1998) description is shown in Figure 3.7b. From Figure 3.7b, Golubev and Frolov (1998) poorly predicts the predict the coordination number for South Pole. However, our results were generated using several significant assumptions. We assume that an object is a grain, and both descriptions of the coordination number assume that the firn grains are spherical. However, from micro-CT scans, the objects are often oblong, stretched, or equilateral (see Figure 3.2). Additionally, the maximum coordination number possible from Golubev and Frolov (1998) is 12; even though much of our data is constrained to <12, a considerable portion extends well beyond. These values may not be real and may be the

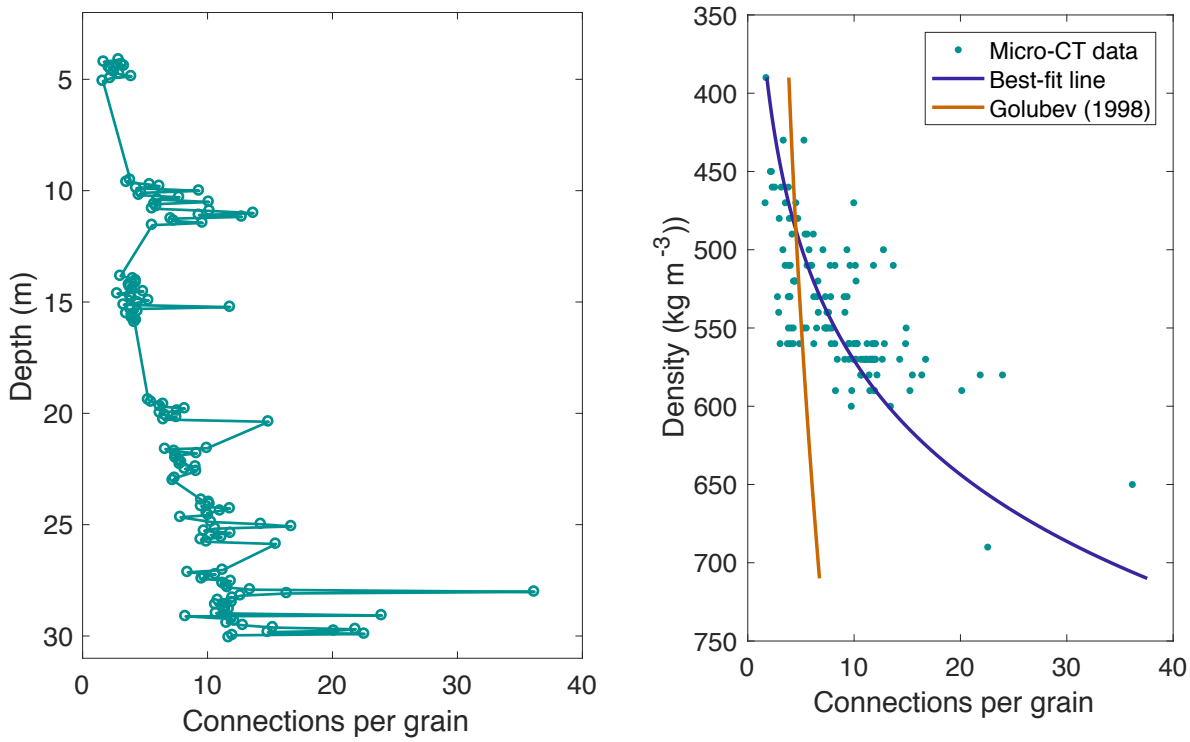

Figure 3.7. (a) Connections per grain evolution with depth. (b) Golubev and Frolov (1998) description of coordination number in comparison with the micro-CT data and the associated best-fit line.

effect of such assumptions. However, if the grains are not spheres but instead have concavities and convexities, they may have the ability to touch more than 12 other grains. Our results provide a first approach for estimating the coordination number, and they suggest the disadvantage in using the spherical-grain assumption and complexity in estimating this parameter in the firn layer.

3.5.3 NECK SIZE

Sintering of firn grains is accompanied by the formation and growth of necks (e.g., Maeno and Ebinuma, 1983). Many mass transport mechanisms contribute to the growth of the necks, including vapor transport, surface diffusion, lattice diffusion, and boundary diffusion

(e.g., Meano and Ebinuma, 1983). Neck size increases as the firn grains become more sintered, so neck size evolution is important for firn densification studies. However, it is not an automatically calculated parameter in the Bruker Micro-CT analyses. We develop an algorithm to calculate neck size from the binary images (similar to Figure 3.2) based on Mandzhieva (2017). Mandzhieva (2017) digitally analyzed cores for pore network modeling and we modify her code to be applicable for our research problem. We first count the white (pores) and black (grains) in our reversed binary images, segment the images using a simple watershed algorithm that computes the Euclidean distance transform to separate the grains and necks. To ensure the images are not oversegmented, we use a different approach from Mandzhieva (2017) and create a mask using the 'imextendedmin' command in Matlab to filter out tiny local minima and use the 'imimposemin' command in Matlab to change the distance transform prohibiting minima from occurring at the filtered-out locations. We label the grains in the image and check whether the pixels are grains or pores, and subsequently estimate the size of the all neck sizes in the binary image through a simple calculation (Mandzhieva (2017)). Figure 3.8 shows an example of a

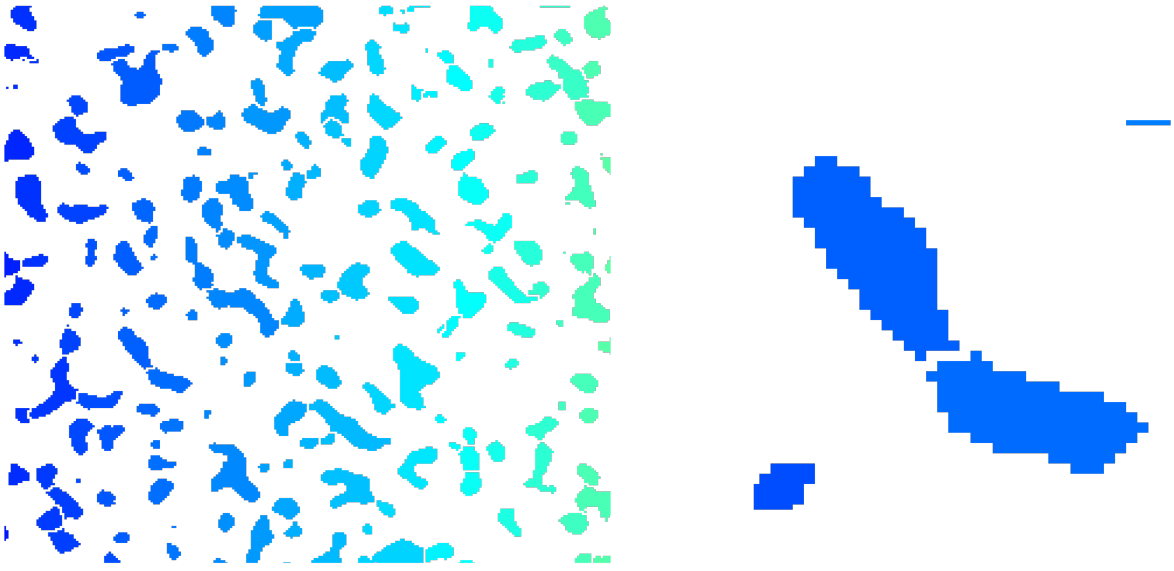

Figure 3.8. (Left) The segmented image is magnified so that individual grains and their predicted necks can be seen. (Right) An object from the segmented image with its predicted neck.

segmented image, and Figure 3.9 shows the spread and shape of the neck size distribution for a sample binary image. To infer the evolution of neck size, we take one representative binary image from the middle (core 5) core of each 1-m section and apply the algorithm. Figure 3.10 shows the estimated evolution of neck size.

The method does not always predict the neck to be at the smallest region of the grain, and a few grains consistently remain unsegmented. Because the grains generally do not show circular shapes, predicting the neck size may not be straightforward to identify as theory from Maeno and Ebinuma (1983) and others have suggested. However, the adjustment of the algorithm's segmentation section does not change the mean neck radii values considerably. Because this is the first algorithm we know of that predicts neck size in micro-CT binary images, this work represents a first step at attempting to approximate this parameter. Future work will be dedicated to improving this algorithm and comparing results with others (e.g., Maeno and Ebinuma, 1983; Hobbs and Mason, 1964).

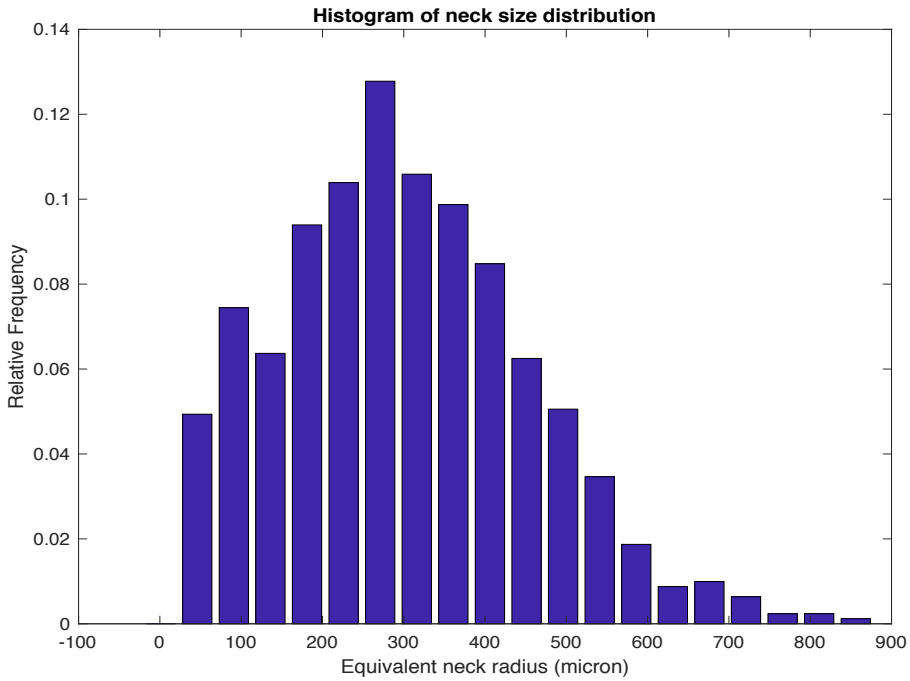

Figure 3.9. An example of the relative frequency of neck radii from a shallow core.

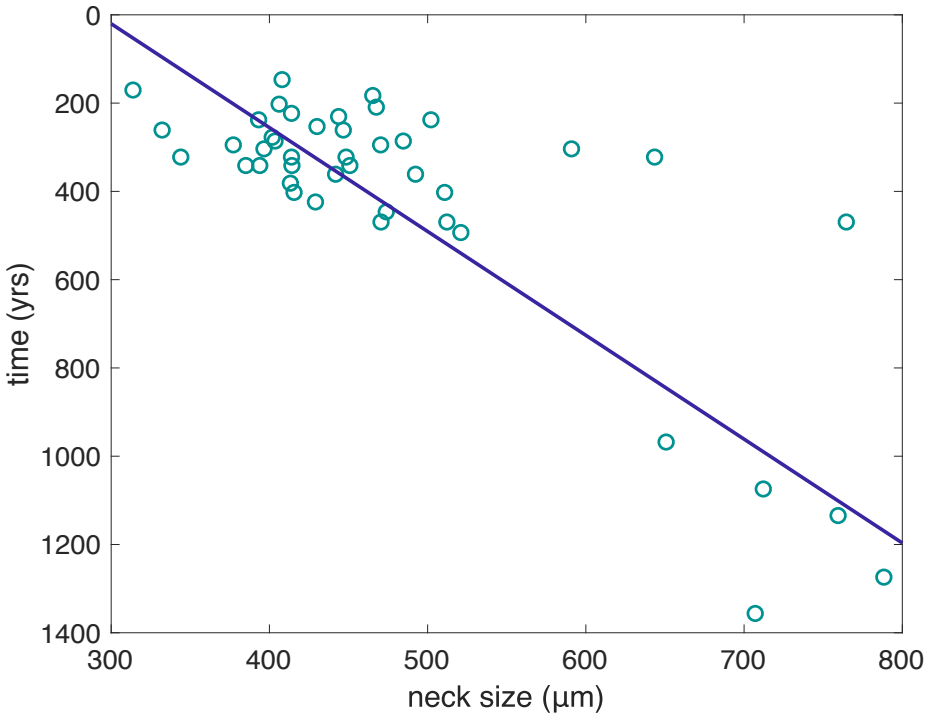

Figure 3.10. The estimated evolution of neck size over the firn core.

3.5.4 FUTURE

The variations of each parameter shown in Figures 3.11. The most notable variations occur at around 26 m in the core, where there is a positive deviation in all three parameters; at around 36 m, where there is a negative deviation in the average object area-equivalent circle diameter and the neck size; and a positive deviation at around 10 m in the connections per grain parameter. Future work will be dedicated to comparing these variations with climate effects at USP50, to expanding the dataset through the entire firn column and reassessing microstructural evolution, and to comparing our results to previous work.

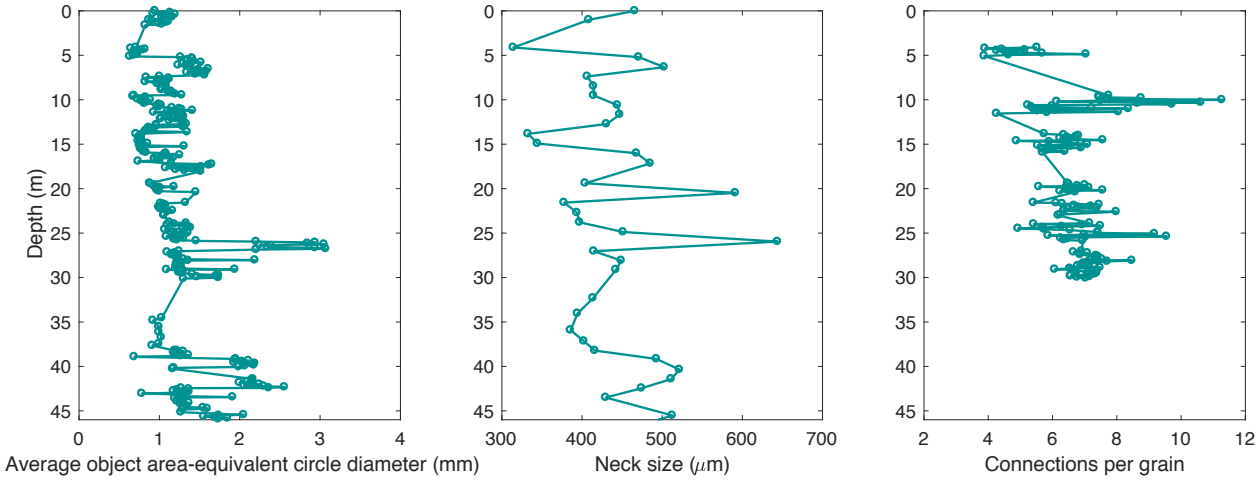

Figure 3.11. Three key microstructure parameters and their variation with depth in the USP50 firn core.

3.6 MODEL OUTPUT

3.6.1 MODELING USP50 FIRN

The Lagrangian framework (Section 3.21), the expression for viscosity η (Section 3.22), the evolution equations from the micro-CT data (Section 3.4), and a constant $v = 1.8 \times 10^{14}$ are used to model the firn layer at USP50. We model from 4 m to 47 m in depth because of the limited range of the data. From Figure 3.12, there is considerable agreement between the data and model. The largest deviation occurs at the extrema of the depth range. The deviation is most likely from calibrating the evolution equations to a limited depth range that our dataset spans.

Figure 3.12 also compares the model to the depth-density profile that the Herron and Langway (1980) model predicts. Because the Herron and Langway (1980) model uses unique densification equations to describe zone 1 (<550 kg m^{-3}) and zone 2 (550 kg m^{-3} - 815 kg m^{-3}), there is an abrupt change in slope in the depth-density curve. The data, and our model, do not show this bend in the depth-density profile. The gradual transition indicates one of the likely strengths for using a model based on microstructural evolution.

Future work will address modeling $\rho >$ 670 kg m^{-3} when the full USP50 firn core is processed for micro-CT data. Other work will involve addressing shortcomings of the model or simplifications that have been made. For example, the model does not account for the changing geometry of the pore spaces or changing anisotropy throughout the firn core. The model also uses simple evolution equations and cannot yet approximate the variations seen in the dataset. However, it is the first known model to use micro-CT data for estimating densification and the depth-density profile for firn. Thus, this model signifies a first step towards attempting to produce a microstructural firn-densification model. These models may, in the future, be able to estimate densification in a wider variety of climate regimes than empirical models. However, the largest disadvantage for this type of model is the availability or data – there are only several sites with micro-CT data and many have been processed with different resolutions, which makes it difficult to compare. Additionally, micro-CT data is difficult to retrieve because of the time and resources it takes to drill and process the firn cores. Thus, the microstructural evolution equations in the model cannot be readily used at other sites. Future work should address laboratory experiments on densifying firn cores while acquiring micro-CT data, which would make obtaining evolution equations easier. However, it is still important to

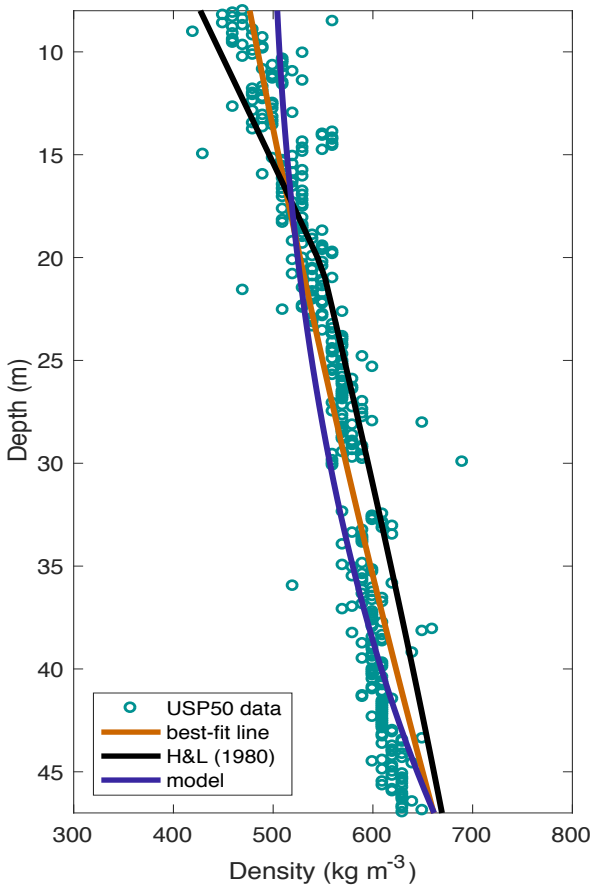

Figure 3.12. The model and data compared to the Herron and Langway (1980) modeled output for South Pole.

explore model output and understand if modeling sites with different climatic conditions is possible using our model. In Section 3.52, we use synthetic microstructure evolution equations compare output with existing depth-density data.

3.6.2 MODELING FIRN IN OTHER CLIMATES

We use the model framework from 3.51 but evolution equations describing microstructural changes that are representative of other climate conditions. To describe grain growth, we use Gow's (1969) formulation that Arthern et al. (2010) also implemented in their model. To define coordination number, we use Golubev's (1998) description. We define the number of objects as exponentially decreasing by using the number of connected objects in the cross section; the neck size as linearly decreasing as a function of pixel size; we assume the orientation of the bonds (that 50% intersect the surface *S*); and assume that the number of bonds intersected by the surface *S* depends on the percent that intersect with surface *S*. The coefficient for grain growth must be adjusted so there exists a stress σ at which the value decreases to 98.8% of the value used in Arthern et al. (2010) for the remaining part of the firn layer.

Our goal is to match the depth-density data with our model output. The following model experiments are for exploring the model capabilities rather than for showing its superiority. Because there are many unknowns, many of the variables can be changed to fit the profile – the constant v, the overburden stress at which the grain growth rate decreases, and the initial values of the microstructural parameters. These values are unconstrained for most sites, so we use estimations to model the climate's depth-density profile. The depth-density data from various sites in Antarctica are shown with the modeled output in Figure 3.13, and were matched by changing the value of the constant v and the overburden stress at which the grain growth rate

changes. The value of the constant v depends on the temperature at the site, and varies linearly as $v = 1\text{x}10^{15}T - 2\text{ x }10^{17}$. The depth at which the growth rate changes and the initial microstructural values can be picked in various combinations to approximate the depth-density data. Thus, these experimental runs show that more data on microstructural parameters is needed to correctly assess firn densification using this model. For example, using an initial grain size of 0.5 mm^2 and a grain growth rate that changes to 98.8% of its original value at $1\text{x}10^{20}$ Pa produces a profile for Dome C that nearly matches the data (see Figure 3.13). Nevertheless, these results show such a firn-densification can exist, and should motivate future work on understanding microstructural evolution in a range of climatic conditions.

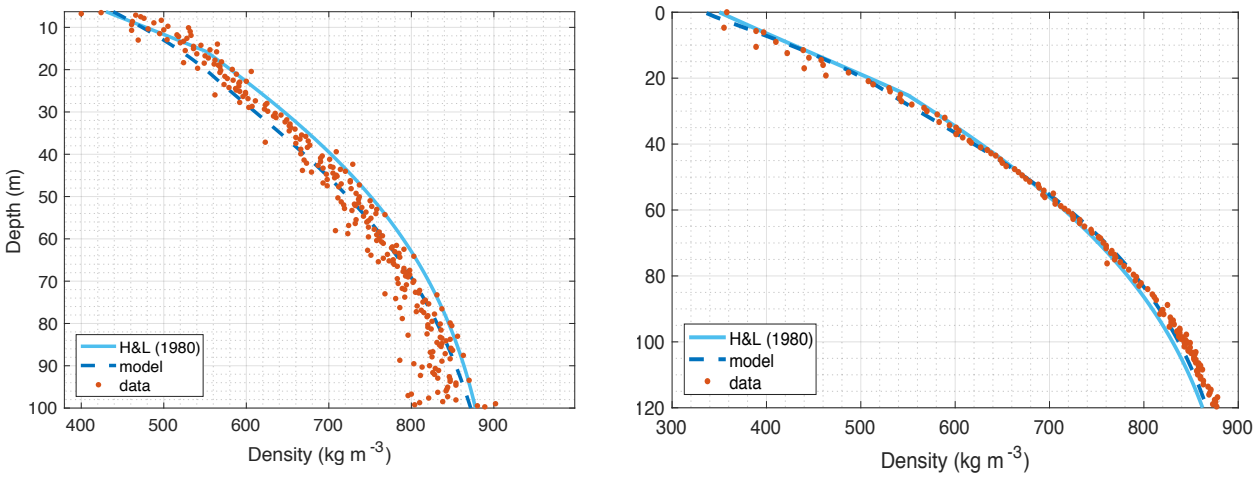

Figure 3.13. Examples of depth-density profiles that compare the modeled output to data. Dome C (left) and Vostok (right).

3.7 CONCLUSION

We developed a firn-densification model based on microstructural evolution by using micro-CT data from USP50 for the upper and transition zone of the firn layer. The model uses a Lagrangian approach by solving microstructural evolution ($D\boldsymbol{s}/Dt$), a viscosity equation that is dependent on the microstructural state ($\boldsymbol{s}$), and then the densification rate ($D\rho/Dt$) during each time step. The viscosity equation is a modification of theory form Feldt and Ballard (1966) to include the effects of grain-boundary sliding and sintering on densification in the upper and transition-zone regions of the firn layer. Microstructural evolution is defined for three parameters (average object area-equivalent circle diameter, coordination number, and neck size) by using the micro-CT dataset of USP50. We compared model output to USP50 for a depth range of 4 m – 47 m. There is agreement between the model and USP50 depth-density data, although more concentrated micro-CT beyond 47 m would likely improve the fit. We also explored the model capabilities by using synthetic microstructure constraints to model the firn layer over a range of climatic conditions, and we compared the output with depth-density data. Our model results are promising and this work represents the first step towards producing a firn-densification model based on microstructural evolution. Continued work should be done to model the entire firn column, to process micro-CT data for the lower USP50 core, and to collect micro-CT at sites with a range of climatic conditions, all of which are essential for advancing model development and for improving our understanding of microstructural evolution in the firn layer.

Chapter 4. CONCLUSION

Modeling firn densification over a wide range of climatic conditions and through changes in climate will most likely require a physically-based model. The commonly-used firn-densification models are empirically constructed, however, and are developed to model the macroscopic properties of the firn layer. Even though a number of studies have addressed physical processes (e.g., grain-boundary sliding) and microstructure (e.g., grain radius) in the firn layer, we still have a poor understanding of the variability of their influence on densification in a wide range of climate conditions and during transient climate. The work presented in this thesis addresses several topics related to this problem.

In Chapter 2, we analyzed the framework and inherent assumptions of a few of the most commonly-used firn-densification models through an implicitly-derived viscosity discontinuity at the zone 1 – zone 2 transition. To generate a continuous viscosity curve while still maintaining an empirical approach, we developed a transition zone firn-densification model that gradually evolves zone 1 processes into zone 2 processes in the transition region around 550 kg m^{-3}, and we compared results to depth-density data and the Herron and Langway (1980) model. We found lower RMSEs for the transition model at sites such as Dominion Range and Ridge B-C, which do not have a regular Clausius-Clapeyron pairing of accumulation rate and temperature. However, at sites such as Ridge B-C, there is a tradeoff between the individual fit over zone 1 and zone 2. These results suggest that the commonly-used firn-densification models are not accurately characterizing fundamental processes important to firn densification, which motivates the development of a physically-based firn-densification model.

In Chapter 3, we developed a firn-densification model based on microstructural evolution. We defined microstructural evolution of three key parameters (average object area-

equivalent circle diameter, neck size, and coordination number) using a micro-CT dataset from the USP50 firn core. Comparing output to USP50 depth-density data, we saw good agreement between the model and data. We also explored the model capabilities at other sites (e.g., Vostok, Dome C) by using synthetic microstructural constraints. This work represents a key step in producing a model based on microstructural evolution. To advance the development of such a model, more data must be collected in a range of climatic conditions to constrain microstructural evolution in the firn layer.

BIBLIOGRAPHY

Alley, RB (1987). Firn densification by grain-boundary sliding: a first model. The Journal of Physics Colloques , 48 (C1), C1-249.

Alley, R. B., Bolzan, J. F., & Whillans, I. M. (1982). Polar firn densification and grain growth. Annals of Glaciology, 3, 7-11.

Anderson, D. L., & Benson, C. S. (1963). The densification and diagenesis of snow.

Arthern, R. J., Vaughan, D. G., Rankin, A. M., Mulvaney, R., & Thomas, E. R. (2010) In situ measurements of Antarctic snow compaction compared with predictions of models. Journal of Geophysical Research: Earth Surface, 115(F3) (doi: 10.1029/2009JF001306)

Arthern, R. J., & Wingham, D. J. (1998). The natural fluctuations of firn densification and their effect on the geodetic determination of ice sheet mass balance. Climatic Change, 40(3-4), 605-624.

Bader, H. (1960). Theory of densification of dry snow on high polar glaciers. U.S. Snow, Ice, and Permafrost Research Establishment. Research Report 69.

Ballard, G. E., & McGaw, R. W. (1965). A theory of snow failure (No. RR-137). Cold Regions Research and Engineering Lab Hanover NH.

Benson, C. S. (1962). Stratigraphic studies in the snow and firn of the Greenland ice sheet (No. RR70). Cold Regions Research and Engineering Lab Hanover NH.

Brown, R. L., Satyawali, P. K., Lehning, M., & Bartelt, P. (2001). Modeling the changes in microstructure of snow during metamorphism. Cold regions science and technology, 33(2-3), 91-101.

Bruker-microCT Analyser: morphometric parameters in 3D and 2D [PDF file].

Community Firn Model. https://github.com/UWGlaciology/CommunityFirnModel

Conway, H., Catania, G., Raymond, C. F., Gades, A. M., Scambos, T. A., & Engelhardt, H. (2002). Switch of flow direction in an Antarctic ice stream. Nature, 419(6906), 465.

Cresseri, S. (2005). Constitutive modelling of dry granular snow at low strain rates.

Cresseri, S., & Jommi, C. (2005). Snow as an elastic viscoplastic bonded continuum: a modelling approach. Italian Geotechnical J, 4, 43-58.

Durand, G., Gagliardini, O., Favier, L., Zwinger, T., & Le Meur, E. (2011). Impact of bedrock description on modeling ice sheet dynamics. Geophysical Research Letters, 38(20).

Edens, M. Q., & Brown, R. L. (1991). Changes in microstructure of snow under large deformations. Journal of Glaciology, 37(126), 193-202.

Feldt, E. D., & Ballard, G. E. H. (1966). A theory of the consolidation of snow. Journal of Glaciology, 6(43), 145-157.

German, R. M. (1996). Sintering theory and practice. Solar-Terrestrial Physics, 568.

Golubev, V. N., & Frolov, A. D. (1998). Modelling the change in structure and mechanical properties in dry-snow densification to ice. Annals of Glaciology, 26, 45-50.

Gow, A. J. (1969). On the rates of growth of grains and crystals in South Polar firn. Journal of Glaciology, 8(53), 241-252.

Gregory, S. A., Albert, M. R., & Baker, I. (2014). Impact of physical properties and accumulation rate on pore close-off in layered firn. The Cryosphere, 8(1), 91-105.

Helsen, M. M., Van Den Broeke, M. R., Van De Wal, R. S., Van De Berg, W. J., Van Meijgaard, E., Davis, C. H., Li, Y., & Goodwin, I. (2008). Elevation changes in Antarctica mainly determined by accumulation variability. science, 320(5883), 1626-1629.

Herron, M. and C.C. Langway (1980), Firn densification: an empirical model. Journal of Glaciology 25(93), 373–385.

Hobbs, P. V., & Mason, B. J. (1964). The sintering and adhesion of ice. Philosophical Magazine, 9(98), 181-197.

Hörhold, M. W., Kipfstuhl, S., Wilhelms, F., Freitag, J., & Frenzel, A. (2011). The densification of layered polar firn. Journal of Geophysical Research: Earth Surface, 116(F1).

IPCC, 2013: Climate Change 2013: The Physical Science Basis. Contribution of Working Group I to the Fifth Assessment Report of the Intergovern- mental Panel on Climate Change [Stocker, T.F., D. Qin, G.-K. Plattner, M. Tignor, S.K. Allen, J. Boschung, A. Nauels, Y. Xia, V. Bex and P.M. Midgley (eds.)]. Cambridge University Press, Cambridge, United Kingdom and New York, NY, USA, 1535 pp.

Kuipers Munneke, P., Ligtenberg, S., Noël, B., Howat, I. M., Box, J. E., Mosley-Thompson, E., ... & Van Den Broeke, M. R. (2015). Elevation change of the Greenland Ice Sheet due to surface mass balance and firn processes, 1960-2014. The Cryosphere, 9(6), 2009-2025.

Le Brocq, A. M., Payne, A. J., & Vieli, A. (2010). An improved Antarctic dataset for high resolution numerical ice sheet models (ALBMAP v1). Earth system science data., 2(2), 247-260.

Ligtenberg, S. R. M., Helsen, M. M., & Van den Broeke, M. R. (2011). An improved semi-empirical model for the densification of Antarctic firn. The Cryosphere, 5(4), 809-819.

Li, J., & Zwally, H. J. (2004). Modeling the density variation in the shallow firn layer. Annals of Glaciology, 38, 309-313.

Li, J., & Zwally, H. J. (2011). Modeling of firn compaction for estimating ice-sheet mass change from observed ice-sheet elevation change. Annals of Glaciology, 52(59), 1-7.

Lundin, J. M., Stevens, C. M., Arthern, R., Buizert, C., Orsi, A., Ligtenberg, S. R, Simonsen, S. B., Cummings, E., Essery, R., Leahy, W., Harris, P., Helsen, M. M., and Waddington, E.

D. (2017) Firn Model Intercomparison Experiment (FirnMICE). Journal of Glaciology, 63(239), 401-422 (doi:10.1017/jog.2016.114.)

Maeno, N., & Ebinuma, T. (1983). Pressure sintering of ice and its implication to the densification of snow at polar glaciers and ice sheets. The Journal of Physical Chemistry, 87(21), 4103-4110.

Mandzhieva, R. (2017). Introduction to digital core analysis: 3D reconstruction, numerical flow simulations and pore network modeling (Master's thesis, NTNU).

Mayewski, P. A., Lyons, W. B., Zielinski, G. A., Twickler, M. S., Whitlow, S. I., Dibb, J. E., ... & Wake, C. P. (1995). An ice-core-based, Late Holocene history for the Transantarctic Mountains, Antarctica.

Morris, E. (2018). Modeling Dry-Snow Densification without Abrupt Transition. Geosciences, 8(12), 464.

Morris, E.M., R. Mulvaney, R.J. Arthern, D. Davies, R.J. Gurney, P. Lambert, J. de Rydt, A.M Smith, R.J. Tuckwell, and M.Winstrup. (2017). Snow Densification and Recent Accumulation Along the iSTAR Traverse, Pine Island Glacier, Antarctica Journal of Geophysical Research Earth Surface https://doi.org/10.1002/2017JF004357.

Morse, D. L., E. D. Waddington, H.-P. Marshall, T. A. Neumann, E. J. Steig, J. E. Dibb, D. P. Winebrenner, and R. J. Arthern (1999) Accumulation rate measurements at Taylor Dome, East Antarctica: techniques and strategies for mass balance measurements in polar environments. Geografiska Annaler: Series A, Physical Geography, 81A(4), 683–694.

Parfitt, A. M., Drezner, M. K., Glorieux, F. H., Kanis, J. A., Malluche, H., Meunier, P. J., ... & Recker, R. R. (1987). Bone histomorphometry: standardization of nomenclature,

symbols, and units: report of the ASBMR Histomorphometry Nomenclature Committee. Journal of bone and mineral research, 2(6), 595-610.

Robin, G. de Q. (1958) Glaciology. Ill. Seismic shooting and related investigations. Norwegian-British-Swedish Antarctic Expedition, 1949-52. Scientific Results, Vol. 5.

Shepherd, A., Ivins, E. R., Geruo, A., Barletta, V. R., Bentley, M. J., Bettadpur, S., ... & Horwath, M. (2012). A reconciled estimate of ice-sheet mass balance. Science, 338(6111), 1183-1189.

Simonsen, S.B., L. Stenseng, G. Adalgeirsdottir, R.S. Fausto, C.S. Hvidberg and P. Lucas-Picher (2013) Assessing a multilayered dynamic firn-compaction model for Greenland with ASIRAS radar measurements. Journal of Glaciology, 59(215), 545–558 (doi:10.3189/2013JoG12J158).

Spencer, M., Alley, R. & Creyts, T. T. (2001) Preliminary firn-densification model with 38-site dataset. Journal of Glaciology, 47(159), 671-676 (doi: 10.3189/172756501781831765)

Wilkinson, D. S. (1988). A pressure-sintering model for the densification of polar firn and glacier ice. Journal of Glaciology, 34(116), 40-45.

Zwally, H. J., & Le, J. (2002). Seasonal and interannual variations of firn densification and ice-sheet surface elevation at the Greenland summit. Journal of Glaciology, 48(161), 199-207.